IRAQI JOURNAL OF APPLIED PHYSICS

The *Iraqi Journal of Applied Physics (IJAP)* is a peer reviewed journal of high quality devoted to the publication of original research papers from applied physics and their broad range of applications. IJAP publishes quality original research papers, comprehensive review articles, survey articles, book reviews, dissertation abstracts in physics and its applications in the broadest sense. It is intended that the journal may act as an interdisciplinary forum for Physics and its applications. Innovative applications and material that brings together diverse areas of Physics are particularly welcome. Review articles in selected areas are published from time to time. It aims to disseminate knowledge; provide a learned reference in the field; and establish channels of communication between academic and research experts, policy makers and executives in industry, commerce and investment institutions. IJAP is a quarterly specialized periodical dedicated to publishing original papers, letters and reviews in: Applied & Nonlinear Optics, Applied Mechanics & Thermodynamics, Digital & Optical Communications, Electronic Materials & Devices, Laser Physics & Applications, Plasma Physics & Applications, Quantum Physics & Spectroscopy, Semiconductors & Optoelectronics, and Solid State Physics & Applications.

EDITORIAL BOARD

Walid K. HAMOUDI
Editor-in-Chief
School of Applied Sciences
University of Technology, IRAQ

Raid A. ISMAIL
Member
School of Applied Sciences,
University of Technology, IRAQ

Dayah N. RAOUF
Member
School of Applied Sciences
University of Technology, IRAQ

Raad A. KHAMIS
Member
School of Applied Sciences
University of Technology, IRAQ

Oday A. HAMADI
Managing Editor
Department of Physics,
College of Education, The Iraqi
University, Baghdad, IRAQ

Rania A. MARKUB
Middle East Coordinator
P. O. Box 55259,
Baghdad 12001, IRAQ

Haitham M. MIKHLIF
Reviews Editor
Department of Physics,
Al-Mustansiriya University, IRAQ

Intesar F. RAMLEY
Industrial Relation Coordinator
INToo Software, Vancouver,
V4B 4W4, BC, Canada

Editorial Office
P. O. Box 55259,
Baghdad 12001,
IRAQ

Email: irq_appl_phys@yahoo.com
Email: editor_ijap@yahoo.co.uk
Tel.: **00964 7901274190**

ADVISORY BOARD

Xueming LIU
Professor
Department of Electronic Engineering,
Tsinghua University, Beijing, CHINA

Mansoor SHEIK-BAHAE
Associate Professor
Department of Physics and Astronomy,
University of New Mexico, U.S.A

Shivaji H. PAWAR
Professor
D. Y. Patil University, Kasaba Bawada,
Kolhapur-416 006, INDIA

Franko KUEPPERS
Professor
College of Optical Sciences,
University of Arizona, Tucson, U.S.A

Yushihiro TAGUCHI
Professor
Department of Physics,
Chuo University, Bunkyo-ku,
Tokyo, JAPAN

El-Sayed M. FARAG
Professor
Department of Sciences, College of
Engineering, Al-Minofiya University, EGYPT

Mutaz S. ABDUL-WAHAB
Assistant Professor
Electric and Electronic Engineering, University
of Technology, Baghdad, IRAQ

Mazin M. ELIAS
Professor
Laser Institute for Postgraduates
University of Baghdad, Baghdad, IRAQ

Kais A. AL-NAIMEE
Assistant Professor
National Institute of Applied Optics, Phys. Dep.,
University of Florence, Florence, Italy

Muhammad A. HUSSAIN
Assistant Professor
Department of Laser and Optoelectronics
Engineering, Al-Nahrain University, IRAQ

Chang Hee NAM
Professor
Korean Advanced Institute of Science
and Technology, Taejon, KOREA

Ashok KUMAR
Professor
Harcourt Butler Technological Institute, Kanpur-
208 002, INDIA

Marc BURGELMAN
Professor
Electronics and Information Systems,
University of Gent, Gent, BELGIUM

Heidi ABRAHAMSE
Professor
Faculty of Health Sciences, University
of Johannesburg, SOUTH AFRICA

Andrei KASIMOV
Professor
Institute of Material Science,
National Academy of Science,
Kiev, UKRAINE

Yanko SAROV
Assistant Professor
Micro- and Nanoelectronic Systems, Technical
University Ilmenau, GERMANY

Mohammed A. HABEEB
Professor
Department of Physics, Faculty of
Science, Al-Nahrain University, IRAQ

Abdullah M. SUHAIL
Assistant Professor
Department of Physics, College of
Science, University of Baghdad, IRAQ

Khaled A. AHMED
Assistant Professor
Department of Physics, College of Science, Al-
Mustansiriya University, IRAQ

Manal J. AL-KINDY
Assistant Professor
Department of Electronic Engineering,
Al-Nahrain University, IRAQ

SPONSORED AND PUBLISHED BY
THE IRAQI SOCIETY FOR ALTERNATIVE AND RENEWABLE ENERGY SOURCES & TECHNIQUES (I.S.A.R.E.S.T.)

www.iraqiphysicsjournal.com, www.facebook.com/editor.ijap, @IJAP2010

IRAQI JOURNAL OF APPLIED PHYSICS

“ INSTRUCTIONS TO AUTHORS “

CONTRIBUTIONS

Contributions to be published in this journal should be original research works, i.e., those not already published or submitted for publication elsewhere, individual papers or letters to editor.

Manuscripts should be submitted to the editor at the mailing address:

Iraqi Journal of Applied Physics, Editorial Board
P. O. Box 55259, Baghdad 12001, IRAQ, admin@iraqiphysicsjournal.com, editor_ijap@yahoo.co.uk

MANUSCRIPTS

Two hard copies with soft copy on a compact disc (CD) should be submitted to Editor in the following configuration:

- **One-column** Double-spaced one-side A4 size with 2.5 cm margins of all sides
- Times New Roman font (16pt bold for title, 14pt bold for names, 12pt bold for headings, 12pt regular for text)
- Letters should not exceed 10 pages, papers should not exceed 20 pages and reviews are up to author.
- Manuscripts presented in English only are accepted.
- English abstract not exceed 150 words
- 4 keywords (at least) should be maintained on (PACS preferred)
- Author(s) should express all quantities in SI units
- Equations should be written in equation form (*italic* and symbolic)
- Figures and Tables should be separated from text
- Figures and diagrams can be submitted in colors for assessment and they will be returned to authors after provide printable copies
- Charts should be indicated by the software used for
- Only original or high-resolution scanner photos are accepted
- For electronic submission, articles should be formatted with MS-Word software.

AUTHOR NAMES AND AFFILIATIONS

It is IJAP policy that all those who have participated significantly in the technical aspects of a paper be recognized as co-authors or cited in the acknowledgments. In the case of a paper with more than one author, correspondence concerning the paper will be sent to the first author unless staff is advised otherwise.

Author name should consist of first name, middle initial, last name. The author affiliation should consist of the following, as applicable, in the order noted:

- Company or college (with department name or company division), Postal address, City, state, zip code, Country name, and Telephone, and e-mail

REFERENCES

The references should be brought at the end of the article, and numbered in the order of their appearance in the paper. The reference list should be cited in accordance with the following examples:

[1] X. Ning and M.R. Lovell, "On the Sliding Friction Characteristics of Unidirectional Continuous FRP Composites", *ASME J. Tribol.*, 124(1) (2002) 5-13.

[2] M. Barnes, "Stresses in Solenoids", *J. Appl. Phys.*, 48(5) (2001) 2000–2008.

[3] J. Jones, "Contact Mechanics", Cambridge University Press (Cambridge, UK) (2000), Ch.6, p.56.

[4] Y. Lee, S.A. Korpela and R. Horne, "Structure of Multi-Cellular Natural Convection in a Tall Vertical Annulus", Proc. 7th International Heat Transfer Conference, U. Grigul et al., eds., Hemisphere (Washington DC), 2 (1982) 221–226.

[5] M. Hashish, "Waterjet Technology Development", High Pressure Technology, PVP-Vol. 406 (2000), 135-140.

[6] D.W. Watson, "Thermodynamic Analysis", ASME Paper No. 97-GT-288 (1997).

[7] C.Y. Tung, "Evaporative Heat Transfer in the Contact Line of a Mixture", Ph.D. thesis, Rensselaer Polytechnic Institute, Troy, NY (1982).

PROOFS

Authors will receive proofs of papers and are requested to return one corrected hard copy with a WORD copy on a compact disc (CD). New materials inserted in the original text without Editor permission may cause rejection of paper.

COPYRIGHT FORM

Author(s) will be asked to transfer copyrights of the article to the Journal soon after acceptance of it. This will ensure the widest possible dissemination of information.

OFFPRINTS

Authors will receive offprints free of charge and any additional offprints can be ordered.

SUBSCRIPTION AND ORDERS

Annual fees (4 issues per year) of subscription are:

- 50 US$ for individuals inside Iraq.
- 100 US$ for establishments inside Iraq.
- 100 US$ for individuals abroad.
- 200 US$ for establishments abroad.

Fees are reduced by 25% for I.S.A.R.E.S.T. members. Orders of issues can be submitted by contacting the editor-in-chief or editorial office at **admin@iraqiphysicsjournal.com** or **editor_ijap@yahoo.co.uk** to maintain the address of issue delivery and payment way.

IRAQI JOURNAL OF APPLIED PHYSICS
المجلــة العراقيــة للفيزياء التطبيقية

Iraqi J. of Appl. Phys., Vol.1, No.1, 2005, 11-14

Optical Response Characterization of In_2O_3/c-Si Prepared by Spray Pyrolysis

Raid A. Ismail (1)
Omar A. A. Sultan (2)

(1) School of Applied Sciences,
University of Technology,
Baghdad, IRAQ
raidismail@yahoo.com

(2) NASSR State Company,
Ministry of Industry and Minerals,
Baghdad, IRAQ
omarsatar2003@yahoo.com

In_2O_3 thin films have been deposited on silicon substrate by chemical spray pyrolysis. These films show high transparency in the visible and near-IR regions. Photoresponse of In_2O_3/c-Si isotype heterojunction detector without post-deposition heat treatment has been investigated in the visible and near infrared regions. Peak response situated at 600nm was observed. External quantum efficiency was 32% at peak response. C-V measurement revealed that the junction was abrupt type and built-in potential around 1 V has been obtained.

Keywords: *Thin Film Heterojunction, Chemical Spray Pyrolysis, Indium Oxide, Silicon-Base Devices*

Received: 20 July 2004, Revised: 24 October 2004, Accepted: 1 November 2004

1. Introduction

The deposition and processing of wide-band gap transparent conductive oxides (TCO's) heterojunctions have become the topic of many recent investigations for next generation of very large area solar cells [1-5]. One of the most important materials of TCO's is indium oxide (In_2O_3). In_2O_3 is a wide-band gap (3.6eV) semiconductor with n-type conductivity. It has a higher value of mobility for free carriers and thus shows better results than those obtained with some other TCO's[6]. Several deposition techniques have been employed for the growth of polycrystalline In_2O_3 films [7]. One of the promising techniques is the chemical spray pyrolysis (CSP) [8]. This technique is low-cost, simple, and reliable. In this technique, high efficient solar cells have been made [9-12]. Recheva *et al.* [13] showed that In_2O_3:(Sn,Te)/n-Si heterojunction position sensitive photodetector (PSP) has good linearity characteristics. In this paper, we report our experimental results on optoelectronics properties of In_2O_3/n-Si heterojunction made by CSP technique. These results are compared with the conventional p-n junction silicon photodiode.

2. Experiment

The starting material used in the present investigation is single crystalline n-type silicon wafers with orientation of (111) and resistivity of 1-3 Ω.cm. They were preliminary cleaned by boiling alcohol and then dried and then etched with dilute HF acid to remove native oxide. The heterojunctions were prepared by spraying 0.4M of an aqueous solution of $InCl_3$ onto mirror-like silicon and glass substrates heated and maintained at 400°C. In_2O_3 thin film formation can be explained by the following chemical reaction:

$$2InCl_3 + 3H_2O \rightarrow In_2O_3 + 6HCl \qquad (1)$$

The experimental set-up of CSP system is presented in Figure (1). The thickness of polycrystalline In_2O_3 film measured by gravimetric method (weighing the substrate before and after film deposition) was about 200nm.

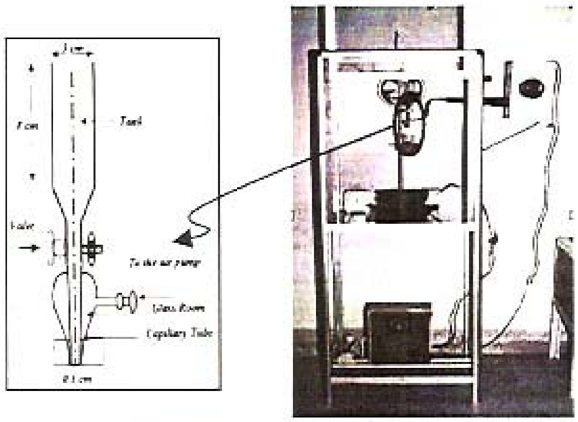

Fig. (1): Experimental Set-up of Spraying Apparatus (Right), and Layout of Enlarged Spraying Glass Nozzle (Left)

The transmittance of the film that deposited on glass substrate was estimated by using spectrophotometer (λ-9) in the range 400-1300nm. Seebeck measurements have been used to investigate the electrical conductivity type of In_2O_3 films. Ag electrode was deposited on

In_2O_3 film and Al electrode was deposited onto the back surface of Si substrate through suitable mask with 450nm thick, using thermal resistive technique. The structure of heterojunction photodetector is shown in Figure (2). The sensitive area of the detector was around 25mm^2. The spectral responsivity at zero bias was measured using monochromator in the range 450-1100nm. The electrical characteristics of the heterojunctions were examined using C-V measurements at frequency of 0.5MHz. Diode laser with wavelength of 904nm and pulse duration of 100ns (FWHM) was used to measure the rise time of photodetector. Storage CRO (100MHz band width) was used to estimate rise time of photodetector.

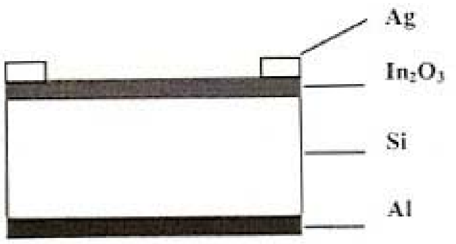

Fig. (2): Cross-sectional view of heterojunction

3. Results And Discussion

Figure (3) presents the transmittance of In_2O_3 films (200nm thick) in the spectral range 450-1000nm. It is obvious that the film exhibits average transparency around 80%, this property acts as window effect for visible and near-IR regions. This property is suitable for silicon photodetector fabrication.

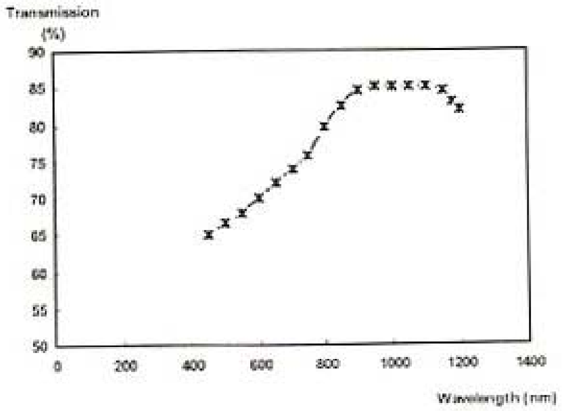

Fig. (3): Transmittance against wavelength curve

The film thickness selected here to exhibits high figure of merit (high T/R) where R is electrical sheet resistance.

Seebeck results showed that conductivity type of In_2O_3 layer was n-type, therefore, isotype heterojunction was formed.

Current-voltage curve (shown in Figure (4)) demonstrates good rectifying behavior, e.g. (rectification factor is about 1250 at 1Volt bias voltage). No soft breakdown is observed in this junction. The I-V under illumination with white light (150mW/cm^2) shows good response and no saturation has been observed.

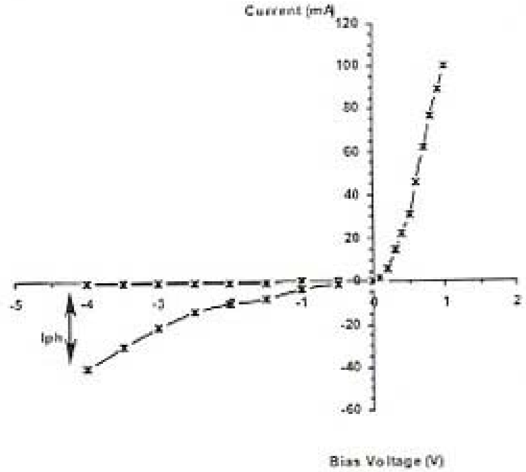

Fig. (4): I-V characteristics in forward and reverse bias under dark and illumination conditions

C-V curve of the isotype heterojunction was shown in Figure (5). This plot confirms that the junction was abrupt type and in good agreement with the standard theory of emission model developed by Anderson [14]. Since the band bending is primarily on the Si side, the C^{-2}-V intercept (not shown here after taking into account the surface capacitance C_o) of 1V on x-axis is essentially equal to the diffusion potential within the Si.

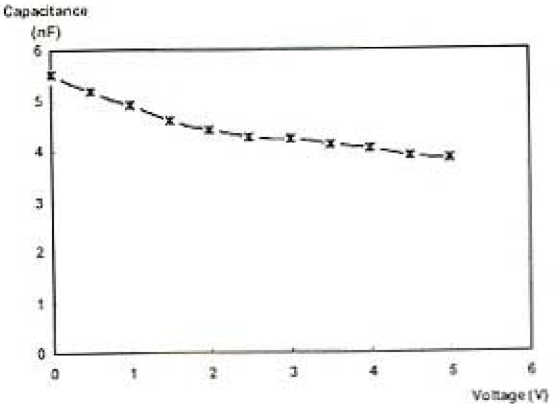

Fig. (5): Capacitance vs. reverse voltage curve

Figure (6) reveals the spectral responsivity plot of hetero-photodiode. It is obvious that the peak response was at 600nm, this is because the band gap of In_2O_3 layer. In contrary to the conventional Si p-n junction photodiode that has peak response at 900±50nm. The shape of responsivity at the low wavelength region depends on the surface condition. Photons of these wavelengths are absorbed at the vicinity of the surface, where they generate charge carrier pairs, which may recombine, before they reach the junction. The recombination reduces carrier availability and consequently the responsivity [15]. On the other hand, it is evident from Figure (5) the responsivity curve has fall-off steeper for short wavelengths than long wavelengths region. For short wavelengths, this effect can be attributed to the parasitic light absorption in the In_2O_3 (via band-to-band transition) [16].

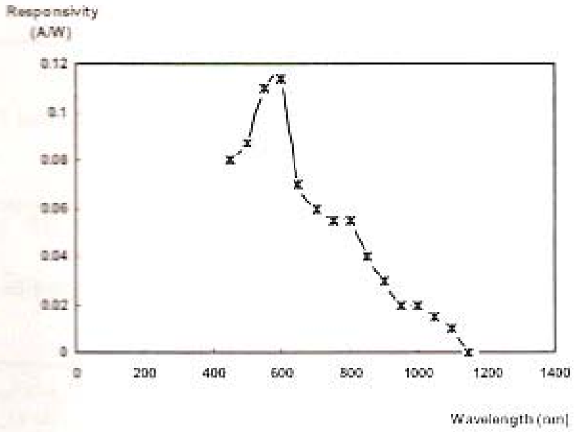

Fig. (6): Spectral responsivity for In_2O_3/c-Si diode

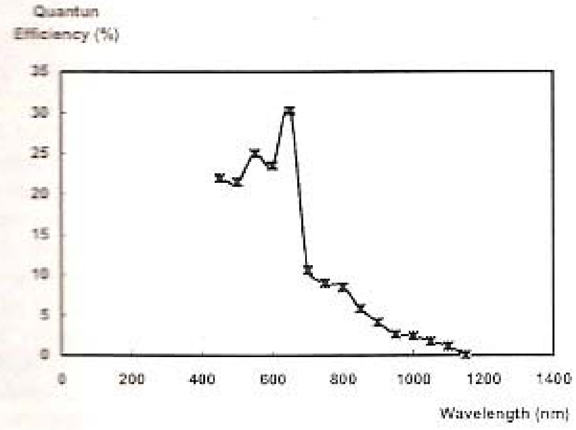

Fig. (7): EQE against wavelength

The external quantum efficiency (EQE) curve is presented in Figure (7). Its maximum value is small in comparison with silicon homojunction and other types of heterojunctions; this is probably due to the interfacial states arises from the defects accompanied the high lattice mismatch between In_2O_3 and Si (about 60%, arising from cubic structure of In_2O_3). The performance of photodiode under specific operating conditions is defined in terms of certain figures of merit. The most important figure of merit is specific spectral detectivity (D). The expression for D of a heterojunction photodiode is given by:

$$D = \frac{\eta\lambda}{2hc}\left(\frac{qA}{I_S}\right)^{1/2} \tag{2}$$

where I_S is saturation current (600nA), A is sensitive area of photodiode, q is electron charge, h is Plank's constant, and c is speed of light.

Figure (8) shows the dependence of D (calculated from equation 1) on the wavelength at 300K. Maximum value of D is comparable to that for diffused silicon.

Time analysis result shows that the rise time of this photodetector is around 50ns and the fall time is longer than 50ns. No significant change in the photodetector main parameters was observed when operating temperature was raised to 60°C, indicating good thermal stability characteristics.

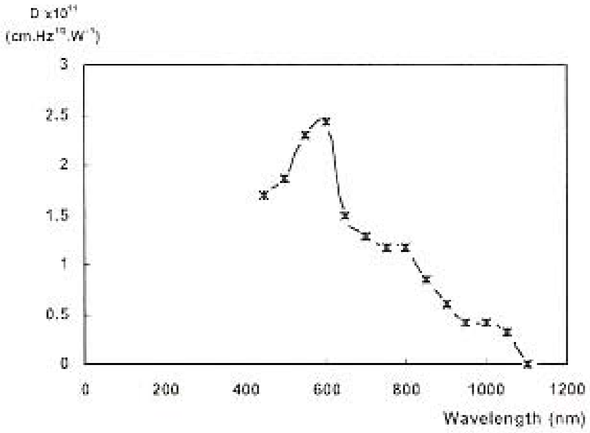

Fig. (8): Specific detectivity as a function of wavelength

4. Conclusions

We have studied elementary characteristics of In_2O_3/Si heterojunction photodiode to provide an economical visible-enhanced photodetector in contrast to silicon homojunction photodiode. The sensitivity to the red line is interpreted to the avoidance of interfacial reactions. These results demonstrate that the In_2O_3/Si heterojunction is a technologically attractive hetero-pairing for the creation of photodiodes applicable in the visible spectral range. Optimization of photodetector performance by controlling the deposition condition of In_2O_3 film is underway.

References

[1] H. Kobayashi et al., *J. Appl. Phys.*, 69, 1736 (1991).
[2] H. Kobayashi et al., *J. Appl. Phys.*, 74, 4756 (1993).
[3] T. Ishida et al., *J. Electrochem. Soc.*, 141, 1357 (1994).
[4] H. Kobayashi etal., *J. Appl. Phys.*, 81, 7630 (1997).
[5] D. Song et al., *17 European PV Conference*, Munich, 2001, p.1.
[6] A. Rasa, P. Agnihotry, B. Gupta, *J. Phys. D: Appl. Phys.*, 10, 1871 (1977).
[7] G. Kiriakidis etal., *Mater. Phys.*, 1, 83 (2000).

[8] S. M. Rozati, M. A. Zanjanch, R. Ghanbarzadeh, World Renewable Energy Congress 7, 29 June-5 July, 2002, Cologne/ Germany.

[9] T. Feng, K. Ghosh, C. Fishman, *Appl. Phys. Lett.*, 35, 266 (1979).

[10] F. Garcra and J. Momuci, *Thin Solid Films*, 97, 47 (1982).

[11] A. Phavdwaj et al., *Solar Cells*, 5, 305 (1982).

[12] R. A. Ismail, A. Alsamar'ai, O. A. Sultan, *J. Eng. Technol.*, 20, 486 (2001).

[13] T. Resheva, V. Vassilev and M. Nanova, *Proc. 12th Conference on Photodetectors*, Bulgaria, 1986, p.275.

[14] R. Anderson, *Solid State Electron.*, 5, 341 (1962).

[15] W. Budde, "**Optical Radiation Measurements**", Academic Press (New York), p.240.

[16] Korzo and Ryabova, *Sov. Phys. Solid States*, 9, 745 (1967).

This article was reviewed at Bulgarian Academy of Science, Bulgaria, University of Hanover, Germany and The University of Technology, Baghdad 35010, Iraq

---

تحضير ودراسة خصائص المفرق In_2O_3/c-Si المصنع بطريقة الرش الكيميائي الحراري

تم ترسيب غشاء In_2O_3 على قاعدة سليكونية بطريقة الرش الكيميائي الحراري. أظهرت هذه الأغشية نفاذية عالية في المنطقتين المرئية وتحت الحمراء القريبة. جرى دراسة الاستجابية الطيفية للثنائي الضوئي المتجانس In_2O_3/Si في المنطقتين المرئية وتحت الحمراء القريبة وبدون إجراء أي تعاملات حرارية بعد التحضير. لقد لوحظ أن قمة الاستجابة تقع عند الطول الموجي 600nm. لقد بلغت الكفاءة الكمية الخارجية عند قمة الاستجابة 32%. كشفت قياسات سعة-جهد أن المفرق من النوع الحاد وإن جهد البناء الداخلي لهذا المفرق حوالي 1eV.

O. Dühr
E.T.J. Nibbering
G. Korn
G. Tempea
F. Krausz

Max-Born-Institut für Nichtlineare Optik und Kurzzeitspektroskopie, Berlin, Germany

Generation of Intense 8-fs Pulses at 400 nm

Frequency-doubled pulses from a sub-40-fs, 1-kHz Ti:sapphire amplifier system are spectrally broadened in an argon-filled hollow waveguide. Compression of the self-phase-modulated pulses is implemented with chirped mirrors and a prism pair, yielding 8-fs, 15-mJ pulses in the violet spectral range.

***Keywords*: Ti:S laser, Femtosecond pulses, Wavelength conversion**

Optical pulse compression has been established as a powerful technique for generating intense sub-10-fs pulses in the red and near-infrared spectral range. Self-phase modulation (SPM) in a single-mode fiber followed by propagation through a dispersive delay line consisting of prisms and diffraction gratings was successfully exploited more than a decade ago for production of 6-fs, 1-nJ, 8-kHz pulses at 620 nm.[1] Recently, further pulse shortening was achieved at higher repetion rates and (or) higher pulse energies. Pulses near 800 nm at a 1-MHz repetition rate with durations as short as 4.5 fs and energies up to 6 nJ were obtained by use of a cavity-dumped Ti:sapphire oscillator and an improved dispersive delay line incorporating chirped mirrors and a prism pair.[2] Replacement of the single-mode fiber with a gas-filled hollow waveguide allowed scaling to much higher pulse energies.[3] SPM in a gas-filled hollow fiber followed by dispersive compression in ultrabroadband chirped dielectric mirrors yielded 4.5–5-fs submillijoule pulses with peak powers up to 0.1 TW at a 1-kHz repetition rate.[4,5]

The generation of intense sub-10-fs pulses was recently extended into the 500–700-nm wavelength range by use of a continuum-seeded noncollinear optical parametric amplifier pumped by the second harmonic of a Ti:sapphire laser.[6,7] To our knowledge, these are the shortest wavelengths at which powerful sub-10-fs light pulses had been produced. In the violet–ultraviolet range microjoule-energy pulses of ~20 fs in duration were demonstrated recently.[8-10] In this Letter we report the generation of 15-μJ, 8-fs pulses at a wavelength of approximately 400 nm.

This experiment draws on our previous work, which resulted in the production of powerful 20-fs pulses tunable from 360 to 440 nm by use of a hollow-waveguide quartz-prism compressor seeded with the frequency-doubled output of a 1-kHz femtosecond Ti:sapphire amplifier system.[10] Pulse shortening was found to be limited by a residual third-order spectral phase left uncompensated in the compressor stage. This system has been improved in several respects. First, shorter frequency-doubled seed pulses with a duration of 29 fs are used. Second, SPM is carefully optimized in the hollow waveguide. Last but not least, the quartz-prism compressor is supplemented with specially designed chirped mirrors that allow reduction of undesirable third-order dispersion (TOD) in the compression system.

Powerful ultrashort pulses at 800 nm are generated with a home-built Ti:sapphire laser system that utilizes chirped-pulse amplification.[11] The seed pulses, as generated by a 15-fs chirped-mirror-compensated Ti:sapphire oscillator,[12] are stretched by a factor of 10,000 in an all-reflective pulse stretcher[13] capable of controlling higher-order dispersion. A lamp-pumped Q-switched intracavity-frequency-doubled Nd:YLF laser delivering an average output power of 23 W at 532 nm pumps a 10-round-trip regenerative Ti:sapphire amplifier and a two-pass Ti:sapphire power amplifier at a repetition rate of 1 kHz. The 2.4-mJ amplified pulses, with a spectrum peaking at 800 nm, are recompressed with a 50%-transmitting reflective grating pair to a pulse duration of 38 fs.

Efficient frequency doubling of downcollimated 1-mJ 38-fs fundamental pulses is achieved in 100-μm-thick β-barium borate (BBO), resulting in violet pulses with energies up to 400 μJ and a spectral width of 8 nm [see Fig. 1(a)]. Changing the distance of the compressor gratings in the amplifier system slightly introduces a small negative chirp in the fundamental that precompensates for dispersion in the doubling crystal and allows us to achieve high conversion efficiencies, up to 40%. Self-diffraction (SD) third-order autocorrelation measurements of the violet pulses in a 100-μm-thick potassium dihydrogen phosphate (KDP)

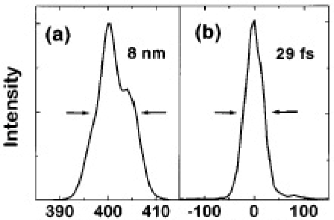

Fig. 1. (a) Spectrum and (b) SD autocorrelation trace of the output of the BBO crystal. A correlation width of 39 fs corresponds to a pulse width of 29 fs.

crystal [Fig. 1(b)] reveal a significantly shorter pulse duration [29 fs (FWHM)] for the second harmonic than for the fundamental.

For spectral broadening, violet pulses of 300-μJ energy are focused with a concave mirror with radius $R = 1$ m into a hollow waveguide with a bore diameter of 220 μm and filled with argon at pressure $p = 0.4{-}0.6$ bars (1 bar = 10,000 Pa). The choice of argon as the nonlinear medium is a good compromise between a moderate ionization threshold and moderate nonlinearity, whereas in the case of helium or neon the ionization properties are better but the nonlinearity is much smaller. Even at these moderate gas pressures the intense light induces strong spectral broadening, as shown in Figs. 2 and 3. We estimate the calculated optimum fiber length L_{opt} for generating a spectrally broadened pulse with a nearly quadratic spectral phase (i.e., linear chirp in the time domain) to be 40 cm for $\lambda_0 = 400$ nm, using $L_{\mathrm{opt}} = (6L_{\mathrm{nl}}L_D)^{0.5}$,[14] where $L_{\mathrm{nl}} = 1/\gamma P_0 = 1.3$ cm and $L_D = T_0{}^2/\beta_2 = 1.9$ m. Here $P_0 = 26$ GW is the peak power of the seed pulses, and $T_0 = 48$ fs is defined by $P(T_0) = P_0/e$. Further, $\gamma = n_2\omega_0/cA_{\mathrm{eff}} = 3.01 \times 10^{-11}$ W^{-1}cm^{-1} is the nonlinear coefficient, $n_2 = 3.10 \times 10^{-19}$ cm^2 W^{-1} is the nonlinear refractive index at $p = 0.6$ bars,[15] A_{eff} is the effective cross-sectional area of the hollow waveguide, and $\beta_2 = 12.41$ fs^2 cm^{-1} is the group-velocity dispersion, including contributions from the waveguide and the argon gas.[16] To introduce some discrimination against higher-order transverse propagation modes, which may also be excited to some extent owing to incomplete matching of the free-propagating input beam to the fundamental EH_{11} mode of the waveguide, we use a 70-cm-long waveguide. The output pulse energy delivered in the fundamental mode amounts to approximately 80 μJ, implying a throughput of 26%. The low throughput is assigned to a low coupling efficiency owing to the elliptic beam profile of the second-harmonic pulse, preventing good mode matching to the EH_{11} mode simultaneously in both transverse directions.

The fiber output is collimated with a concave aluminum mirror with $R = 2$ m and reflected six times off chirped multilayer mirrors consisting of 42 alternating layers of $\mathrm{SiO_2}$ and $\mathrm{Ta_2O_5}$. The mirrors exhibit high reflectivity from 330 to 460 nm and are expected to introduce a nearly constant group-delay dispersion (GDD) of approximately -20 fs^2 from 350 to 430 nm. We show a theoretical estimate of the GDD and the TOD in Fig. 2. Employing these chirped mirrors with negligible TOD and minimizing the optical path length in the prisms allows us to reduce the prism apex distance of 45 cm, compared with 130 cm in our previous experiment.[10] Although the dispersion characteristics of the mirrors have still to be measured, we deduce from the shorter prism distance that the mirrors introduce the amount of GDD per bounce that was predicted. The exclusive use of chirped mirrors for pulse compression is currently prevented by the low dispersion and the high loss (10%) that they introduce per bounce. The origin of this anomalously high reflection loss under exposure to high peak intensities remains to be found.

Figure 3 summarizes the results of a SD frequency-resolved optical gating (FROG) measurement[17] of compressed pulses generated at an argon pressure of $p = 0.4$ bars. Figures 3(a) and 3(b) depict the spectrum and the measured SD correlation (filled circles) of the compressed pulses, respectively. The measured SD FROG trace is shown in Fig. 3(c). Figure 3(d) plots the retrieved intensity (solid curve) and phase (dashed curve) of the pulse, yielding a pulse duration (FWHM) of 13 fs and a small amount of residual phase at the pulse center.

The shortest pulse was generated by an increase in pressure of 0.6 bars, which led to further spectral broadening, as revealed by Fig. 4(a). A slight readjustment of the amount of glass introduced by the first prism proved necessary for optimum pulse compression. The SD trace of the compressed pulses [Fig. 4(b)] results in a third-order autocorrelation width of less than 11 fs. We recorded this trace with the stringent requirement of acquisition by use of only those pulses for which the energy and bandwidth fluctuations were less than ±5% of the average value. This excludes any erroneous broadening of the signals owing to intensity fluctuations of the seed pulse. Unfortunately, however, we have not yet implemented these stringent requirements in the acquisition of FROG traces. To determine the deconvolution factor

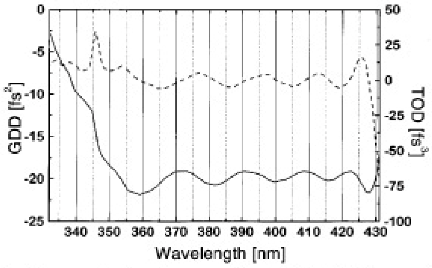

Fig. 2. Theoretical estimate of the GDD (solid curve) and the TOD (dashed curve) properties of the chirped mirrors.

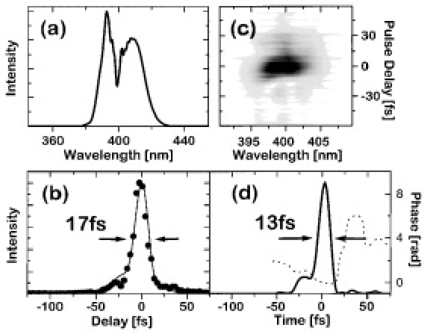

Fig. 3. (a) Spectrum, (b) SD autocorrelation, (c) SD FROG, and (d) retrieved pulse intensity and phase of compressed blue pulses obtained with 0.4-bar Ar in the hollow fiber. A calculated SD trace [solid curve in (b)] compares well with the experimental values (filled circles).

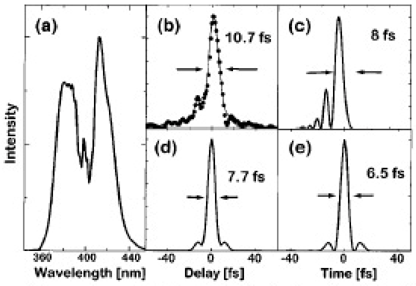

Fig. 4. SD autocorrelation [filled circles in (b)] of compressed blue pulses obtained with 0.6-bar Ar in the hollow fiber with the spectrum given in (a). The solid curves in (b) and (c) are the calculated SD signal- and pulse-intensity profiles, respectively, as described in the text. The Fourier-transform-limited SD signal and the temporal intensity profile are shown in (d) and (e), respectively.

and the residual higher-order phase, we can analyze the compressed pulses only by a fit of the spectral phase,

$$\Phi(\omega) = \Phi_0 + \left.\frac{\mathrm{d}\Phi}{\mathrm{d}\omega}\right|_{\omega_0} (\omega - \omega_0) + \frac{1}{2}\left.\frac{\mathrm{d}^2\Phi}{\mathrm{d}\omega^2}\right|_{\omega_0} \times (\omega - \omega_0)^2 + \frac{1}{6}\left.\frac{\mathrm{d}^3\Phi}{\mathrm{d}\omega^3}\right|_{\omega_0} (\omega - \omega_0)^3 + \dots ,$$

where the second- and third-order Taylor expansion coefficients are to be chosen to provide the best fit to the measured SD autocorrelation trace in Fig. 4(b). This fit is obtained with

$$\left.\frac{\mathrm{d}^2\Phi}{\mathrm{d}\omega^2}\right|_{\omega_0} = 0\ \mathrm{fs}^2, \qquad \left.\frac{\mathrm{d}^3\Phi}{\mathrm{d}\omega^3}\right|_{\omega_0} = -70\ \mathrm{fs}^3.$$

The corresponding pulse intensity envelope and the third-order autocorrelation trace are shown by the solid curves in Figs. 4(c) and 4(b), respectively. The small deviations between the experimental and the calculated traces may be due to higher-order phase terms. It is, however, clear that the remaining spectral cubic phase dominates the pulse characteristics. This analysis results in a pulse duration of 8 fs and a deconvolution factor of 1.35. These values are smaller than those obtained with second-harmonic autocorrelation because of the higher-order nonlinearity $[\chi^{(3)}]$ that is responsible for self-diffraction. The pulse energy after compression is 15 μJ, giving rise to a peak power of approximately 2 GW. Owing to the diffraction-limited nature of the waveguide output, these pulses are expected to be focusable to intensities greater than 10^{16} W/cm^2 with $f/3$ optics.

The intensity envelope and the corresponding SD autocorrelation trace of a transform-limited signal with the spectrum shown in Fig. 4(a) are depicted in Figs. 4(e) and 4(d), respectively. The presence of small satellites relates to the modulated structure of the spectrum. Comparison of Figs. 4(c) and 4(e) implies that the compressed 8-fs violet pulses are 1.25 times Fourier limited.

We have demonstrated the generation of sub-10-fs gigawatt peak-power pulses in the violet spectral range for what we believe to be the first time. The performance of the system is currently limited by the loss and dispersion characteristics of the available chirped mirrors, which have been used in this wavelength range for what is to our knowledge the first time. The hollow-waveguide technique employed for SPM is not restricted to the pulse energies and spectral bandwidths demonstrated in this Letter. In fact, we recently achieved spectral broadening to bandwidths in excess of 70 nm near 400 nm with this same setup. Hence progress in short-wavelength chirped-mirror technology holds promise for the generation of intense 5-fs-scale light pulses in the violet–blue spectral range.

The authors are grateful to K. Ferencz of the Research Institute for Solid State Physics in Budapest for manufacturing the chirped mirrors and A. Nazarkin of the Max-Born-Institut in Berlin for helpful discussions. This research was partly supported by Austrian Science Fund grant Y44-PHY.

References

1. R. L. Fork, C. H. Brito Cruz, P. C. Becker, and C. V. Shank, Opt. Lett. **12,** 483 (1987).
2. A. Baltuška, Z. Wei, M. S. Pshenichnikov, and D. A. Wiersma, Opt. Lett. **22,** 102 (1997).
3. M. Nisoli, S. De Silvestri, and O. Svelto, Appl. Phys. Lett. **68,** 2793 (1996).
4. M. Nisoli, S. De Silvestri, O. Svelto, R. Szipöcs, K. Ferencz, C. Spielmann, S. Sartania, and F. Krausz, Opt. Lett. **22,** 522 (1997).
5. S. Sartania, Z. Cheng, M. Lenzner, G. Tempea, Ch. Spielmann, F. Krausz, and K. Ferencz, Opt. Lett. **22,** 1562 (1997).
6. G. Cerullo, M. Nisoli, and S. De Silvestri, Appl. Phys. Lett. **71,** 3616 (1997).
7. A. Shirakawa, I. Sakawe, and T. Kobayashi, in *Conference on Lasers and Electro-Optics*, Vol. 6 of 1998 OSA Technical Digest Series (Optical Society of America, Washington, D.C., 1998), postdeadline paper CPD11.
8. S. Backus, J. Peatross, M. M. Murnane, and H. C. Kapteyn, Opt. Lett. **21,** 665 (1996).
9. C. G. Durfee III, S. Backus, M. M. Murnane, and H. C. Kapteyn, Opt. Lett. **22,** 1565 (1997).
10. E. T. J. Nibbering, O. Dühr, and G. Korn, Opt. Lett. **22,** 1335 (1997).
11. D. Strickland and G. Mourou, Opt. Commun. **56,** 219 (1985).
12. A. Stingl, M. Lenzner, Ch. Spielmann, F. Krausz, and R. Szipöcs, Opt. Lett. **20,** 602 (1995).
13. B. E. Lemoff and C. P. J. Barty, Opt. Lett. **18,** 1651 (1993).
14. W. J. Tomlinson, R. H. Stolen, and C. V. Shank, J. Opt. Soc. Am. B **1,** 139 (1984).
15. H. J. Lehmeier, W. Leupacher, and A. Penzkofer, Opt. Commun. **56,** 67 (1985).
16. A. Dalgarno and A. E. Kingston, Proc. R. Soc. London Ser. A **259,** 424 (1966).
17. R. Trebino, K. W. DeLong, D. N. Fittinghoff, J. N. Sweetser, M. A. Krumbügel, B. A. Richman, and D. J. Kane, Rev. Sci. Instrum. **68,** 3277 (1997).

Influence of Deposition Parameters on Optical and Electrical Properties of Cu_xS Thin Films Prepared Using Chemical Bath Deposition Method

Ali M. Mousa [1*]
Samir H. Nasher [1]
Jean-Pierre Ponpon [2]

[1] *Material Research Unit,*
School of Applied Science,
University of Technology,
Baghdad, Iraq
* *alzyhery2000@yahoo.com*
[2] *InESS, Umr 7163, CNRS,*
Université Louis Pasteur,
Strasbourg, France

Thin films of Cu_xS have been deposited in an aqueous solution of copper chloride, tri ethanol amine, aqueous ammonia and thiourea. The effect of deposition time, solution pH and thiourea amount on films thickness, growth rate, optical and electrical properties has been studied. The film thickness increases with increasing deposition time and thiourea volume, whereas it decreases with increasing the solution pH. The corresponding small modifications of optical properties can be explained by the increase in roughness with film thickness. Electrical resistivity is strongly influenced by the solution pH and by the thiourea amount but depends to a much less extent on the film thickness.

Keywords: Cu_xS, Chemical bath deposition, Optical properties, Electrical properties
Received: 28 April 2008, Revised: 17 August 2008, Accepted: 24 August 2008

1. Introduction

Cu_xS exists in many different phases depending on the ratio of Cu in the compound, but the most important phase is the chalcocite with x=2. The material has a direct band gap of 2.26eV and an indirect gap of about 1.15eV and presents acceptor conductivity. Copper sulfide Cu_2S is a highly photoconductive wide band gap semiconductor and has been considered as an attractive material for solar cells, especially in association with CdS, giving efficiency close to 10% [1]. Cu_2S has also been used with polycrystalline conductive polymer [2].

Cu_2S thin polycrystalline layers have been deposited using many different techniques [3]. Among these Chemical Bath Deposition (CBD) is the cheapest one. It allows one to control the deposition process on different substrates with good stoichiometry [4-7]. The basic principle for CBD of Cu_xS requires the presence of both constituent ions i.e. Cu^{2+} and S^{2-}. The sulfide ions can be produced by the hydrolysis of the thiourea in a basic medium with pH=10-12 or in aqueous NH_3 [8], while the copper ions can be supplied by dissolved copper salts like ($CuCl_2.2H_2O$) [9-11]. When the copper salt is dissolved it gives first $Cu(H_2O)^{+2}$ and the formation of a complex follows. In the case of using NH_3 instantaneous transformation takes place: $Cu(NH_3)(H_2O)_5$ is transformed to the compound $Cu(NH_3)_4(H_2O)^{2+}$. In most published works Cu_xS is deposited from a solution of NH_3, $(NH_2)_2SC$ and $(CH_2CH_2OH)_3N$, where complex ions of $\{Cu(TEA)_n\}^{2+}$ or $\{Cu(NH_3)_m\}^{2+}$ and $\{Cu_4(TU_6\}^{4+}$ will be present, with relative concentrations changing with time of deposition process. The deposition of Cu_xS takes place when the ionic production of Cu^{+2} and S^{-2} is greater than the dissolving rate of Cu_xS.

In this work, we have studied the effect of the deposition parameters (deposition duration, thiourea amount, solution pH) on the optical and electrical properties of Cu_xS thin films prepared by CBD and determined by the values of deposition rates.

2. Experiment

The samples studied in this work were thin polycrystalline films of Cu_xS deposited by CBD on glass substrates with dimensions of 1x26x76 mm^3. Prior to deposition, the substrates were washed with distilled water in ultrasonic bath and then immersed for 24 hours in chromic acid (1gm of CrO_3 in 20ml of distilled water) and finally washed again with distilled water.

The total volume of the deposition bath was 50ml and made from 10ml of the following constituents:

1: $CuCl_2.2H_2O$ (0.5 mol/L);
2: TEA $(CH_2CH_2OH)_3N$ (9.4 mol/L);
3: NH_3 (30%);
4: Thiourea $(NH_2)_2CS$ (1 mol/L);
5: Double distilled water.

For a few experiments the volume of thiourea was adjusted between 5ml and 20ml. The volume of distilled water was modified consequently to maintain a constant 50ml total volume. All depositions were carried out at 30°C. The pH was adjusted between 9 and 13. The substrates were immersed vertically in the bath for times up to 4 hours. After deposition the samples were washed in distilled water and left to dry.

The crystallographic properties of the deposited films were determined by the X-ray diffraction technique using Cu-Kα radiation and scanning 2Θ in the range 10°-60°.

For optical measurements one side of the substrates was cleaned by using H_2SO_4 to remove the deposited layer. Thickness measurement was done by optical method using He-Ne laser light at an incident angle of 45°. The film thickness (t) was calculated using [12]:

$$t = \frac{\lambda}{2} . \frac{\Delta x}{x} \qquad (1)$$

where Δx is the width of the dark fringes and x is the width of light fringes

Optical transmission and absorption measurements were performed at room temperate in the 400-900nm range using a Lambda-9 Perkin-Elmer UV/Visible/NIR spectrophotometer. Values of the energy gap (E_g) were calculated from the extrapolated intercept of $(\alpha h\upsilon)^2$ versus $h\upsilon$, and absorption coefficient was calculated from transmission spectra using Beer-Lamberts law:

$$\alpha = 2.303 \frac{A}{t} \qquad (2)$$

where A is the absorbance

The Reflectance (R) has been found by using the relationship

$$R+T+A = 1 \qquad (3)$$

For electrical measurements two Aluminum electrodes in a coplanar configuration of 5mm width separated by 5mm were evaporated in vacuum on the surface of the deposited films. The Resitivity (R) was simply obtained by calculating the value of the dark resistance and using the relationship

$$R = \rho\ (L/A) \qquad (4)$$

3. Results and discussion

As shown in Fig. (1) representing a typical X-ray diffraction spectrum with only a very broad peak, the prepared films are made of randomly distributed crystallites with amorphous phase. This result is in good agreement with previous results published on films prepared in the same way [6] and as deposited from acidic solution [13].

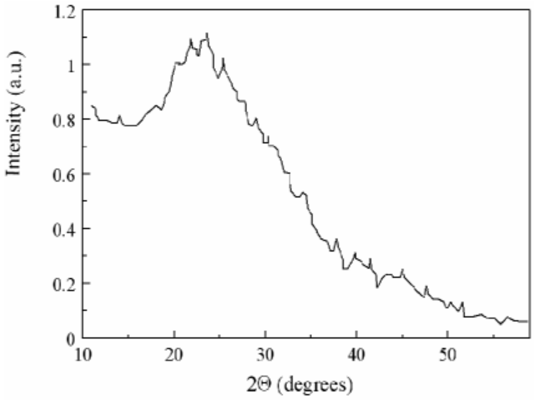

Fig. (1) Typical XRD spectrum of a Cu_xS film deposited by CBD

Fig. (2) depicts the film thickness variation as a function of deposition time, thiourea volume and pH value. Fig. (2a) shows that thickness increases linearly with the deposition time. The deposition rate is nearly constant and equal to 40.3nm per hour, such deposition rate is much greater than those obtained by chemical deposition [13], which need 8h to deposit a film of thickness (100nm) and no sign of saturation is noticed.

Fig. (2b) shows the dependence of the deposited film thickness on thiourea volume at a fixed deposition time (2hrs) and pH=11. Doubling the thiourea volume from 10ml to 20ml is accompanied by a thickness increase from 158nm to 233nm. Such an increment can be attributed to the increase in the number of S^2 in the thiourea volume which accelerates the reaction forming Cu_xS. Clearly, the deposition rate increases with the thiourea volume: it is 68.5nm/hour for 5ml, 79nm/hour for 10ml and becomes 117nm/hour for 20ml, while with using acidic bath the thickness increase quasi linear up to 0.3M and thickness of (200nm) and with more molarities saturation takes place. As shown in Fig. (2c), increasing the pH value at a fixed deposition time (2hrs) results in the thickness decrease. Although the effect on the deposition rate is smaller than in the two former cases, the influence of pH on the deposition rate is clear: starting with 87nm/hr at pH=9 it is only 62nm/hr at pH=13. Such a reduction can be due to the increase in the copper ions concentration (which is a function of the pH value).

Fig. (3) shows the spectral reflectance of four samples deposited for different times at constant pH and thiourea volume (pH=11, thiourea volume=10ml). For wavelengths shorter than 600nm the effect of deposition time is low. In contrast to higher wavelengths the reflectivity increases noticeably with increasing the deposition time. The same evolution can be observed for samples deposited at different pH values and different thiourea volumes. Although the influence of the increase of the number of free carriers cannot be ruled out, it is more likely that this effect results from the increase in the film roughness with thickness.

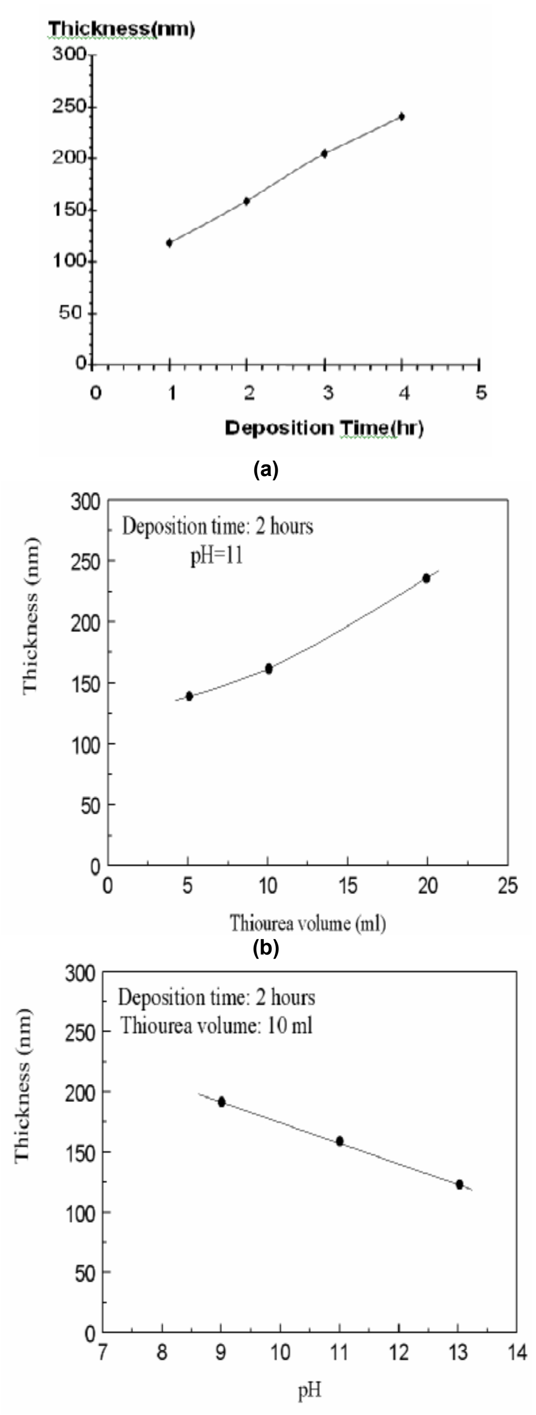

(a)

(b)

(c)

Fig. (2) Evolution of film thickness with (a) deposition time (b) thiourea volume (c) pH

The change in the absorption coefficient in the spectral range 400-900nm is depicted in Fig. (4) as a function of deposition time, thiourea volume and pH value, respectively. Only small differences appear depending on the experimental conditions. For wavelengths longer than 600nm these differences remain within the error limit. In the 400-600nm range, it follows by considering Fig. (2) that the thicker the film the lower the absorption coefficient.

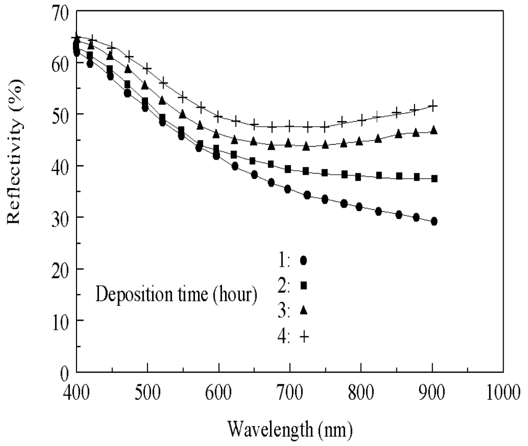

Fig. (3) Spectral dependence of the reflectivity with the deposition time (thiourea volume is 10ml, pH=11)

In any case the differences remain small. This result suggests the effect of some increase in film roughness with thickness actually the absorption coefficient is determined by the mean thickness of the film but the experimentally measured thickness is given by the maximum film height (which includes roughness). Therefore, according to relation 2 and assuming no change of the absorption coefficient throughout the whole thickness (due for example to a significant change in the film composition), overestimation of the film thickness used to calculate α leads to an underestimation of the absorption coefficient. This hypothesis is in agreement with the reflectivity behavior shown in Fig. (3). (Still it has to be remarked that a simple calculation shows that the optical effect of a significant roughness is equivalent to a change of the absorption coefficient in a more or less thin surface layer).

The band gap was calculated from the plot of $(\alpha h\nu)^2$ versus $(h\nu)$ Fig. (5) by using the values of the absorption coefficient. Except for the case of samples deposited for 1 hour (for which E_g=2.4eV), the value of the bandgap is 2.29eV, independent of the preparation conditions. These values differ from those obtained by chemical deposition with E_g=2.48eV for Cu_2S and 2.11eV for $Cu_{1.76}S$ [13].

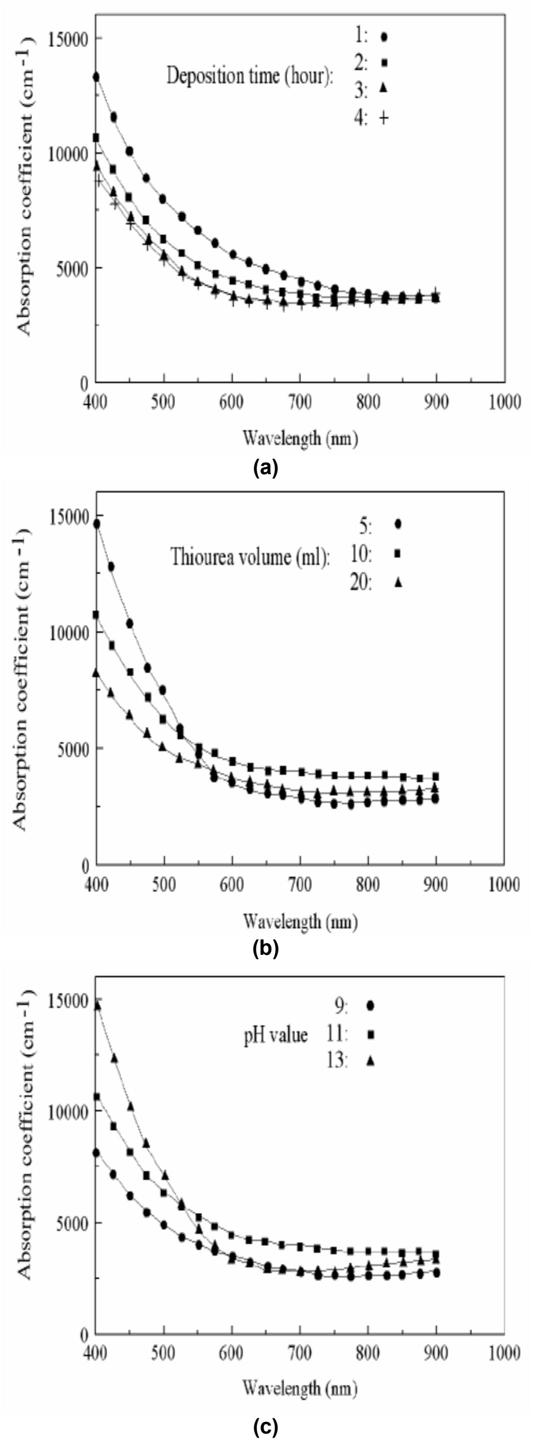

(a)

(b)

(c)

Fig. (4) Spectral dependence of the absorption coefficient with (a) deposition time (b) Thiourea volume (c) pH

The indirect bandgap value is not affected by the deposition time. Its value is 1.16eV for 10ml thiourea and pH=11. Increasing the thiourea volume decreases the indirect bandgap value (1.1eV for 20ml). On the other hand, increasing the pH increases the indirect bandgap (1.6eV for pH=13).

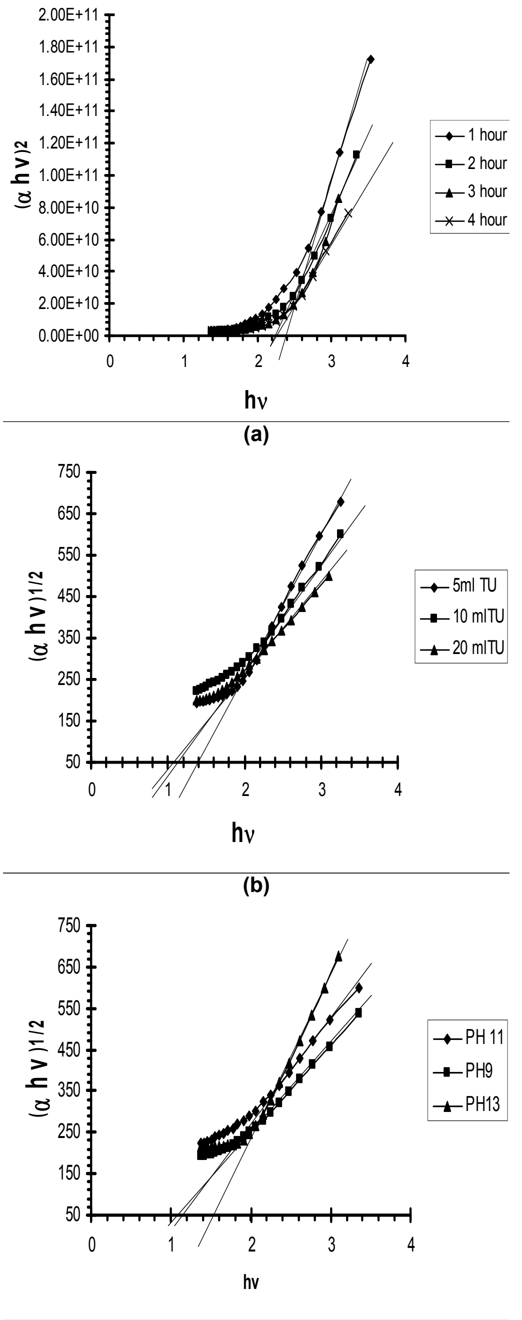

(a)

(b)

(c)

Fig. (5) The plot of $(\alpha h\upsilon)^2$ versus ($h\upsilon$) for different deposition conditions (a) deposition time (b) Thiourea volume (c) pH

Fig. (6) shows the variation in the electrical resistivity as a function of deposition conditions. For pH=11 and thiourea volume=10ml, the resistivity is almost independent of the deposition time up to 3 hours (Fig. 6a). This result is consistent with former results obtained for films deposited by CD [14] but, as already reported, is in sharp contrast with the resistivity increase as a function of deposition time of evaporated Cu_xS thin films [15]. For 4hrs deposition time the resistivity decreases by a factor of two or three. As shown in Fig. (6b), increasing the thiourea volume produces copper sulfide films which reach a very low resistivity (<0.03Ω.cm). In contrast, increasing the pH leads to a nearly exponential increase of the film resistivity (Fig. 6c).

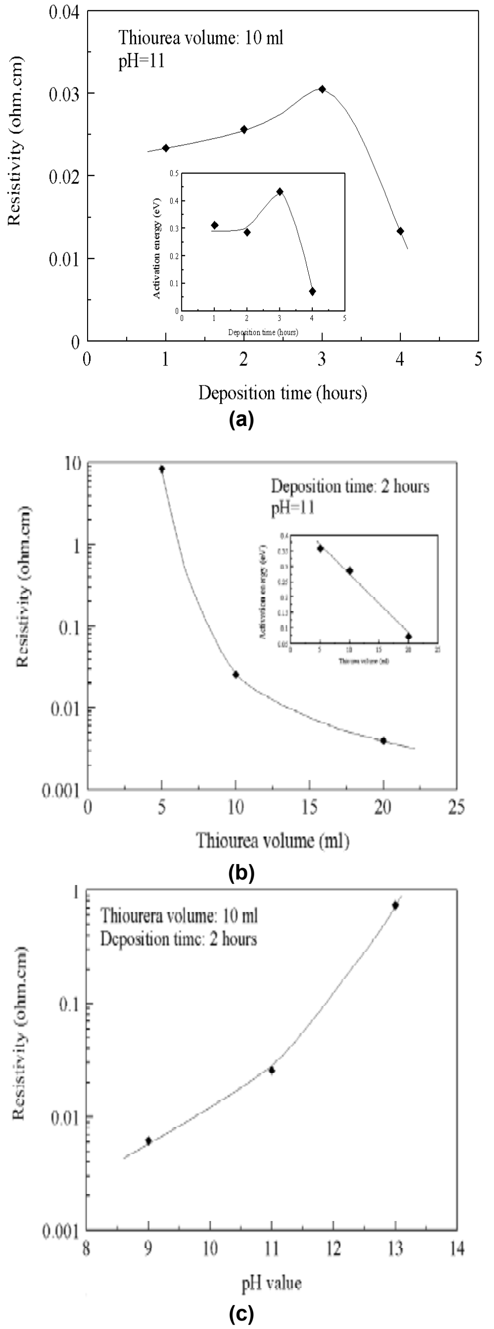

Fig. (6) Change in resistivity as a function of (a) deposition time (the insert shows the variation of activation energy of conductivity) (b) Change in resistivity as a function of thiourea volume (the insert shows the variation in activation energy of conductivity) (c) Change in resistivity as a function of pH

Determination of the activation energy of conductivity at different deposition conditions Table (1) by measuring the variation in the current *I* as a function of temperature *T* and plotting ln(*I*) *vs.* (1/*T*) as shown in Fig**.** (7), allows one to explain most of the previous results by considering an increase in the concentration of acceptor copper vacancies when increasing either thiourea volume or deposition duration. The insert of figure 5b for example shows the variation in the activation energy with thiourea volume for pH=11 and 2 hours deposition time. For the larger thiourea volume, the activation energy tends to go towards 0.07eV, which corresponds to the energy of the V_{Cu} level. The same holds for the influence of deposition time: up to 3hrs, the change in activation energy is low (0.3-0.4eV), insert of Fig. (6a).

Table (1) shows the values of activation energy as a function of deposition conditions

Sample	t_{dep} (hr)	pH	$V_{thiourea}$ (ml)	R (Ω.cm) $x10^{-3}$	E_a (ev)
1	1	11	10	23.387	0.312
2	2	11	10	25.6313	0.286
3	3	11	10	30.5347	0.433
4	4	11	10	13.3317	0.0712
5	2	11	5	8405.4	0.357
6	2	11	20	3.967	0.0723
7	2	9	10	6.18	0.099
8	2	13	10	737.8	0.078

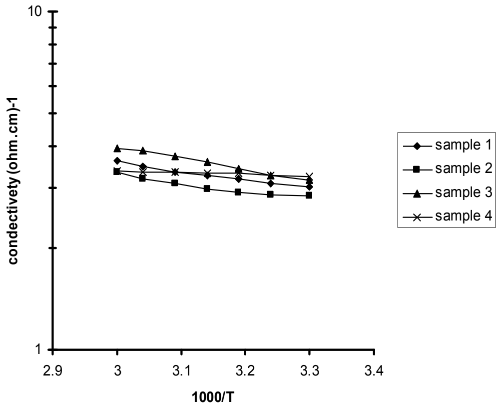

Fig. (7) The conductivity vs. temperature for 4 different samples

However, for 4hrs, the activation energy falls down to 0.07eV. Therefore, one can suppose that the resistivity decrease which is observed for long deposition time and large thiourea volume is induced by the creation of excess copper vacancies which give rise to a large number of free holes. Actually, as thiourea is the source for sulphur, one can expect a larger concentration of copper vacancies (equivalent to a stoichiometry deviation) with increasing the amount of thiourea. On the other hand, the large increase in resistivity with pH can be attributed to a deviation from stoichiometry due to the enhancement of the concentration of copper ions (related to the pH value, as already noticed).

4. Conclusion

Cu_xS films of a few hundreds of nanometer thickness have been prepared by chemical bath deposition for 1 to 4 hours. The film thickness increases with increasing deposition time and thiourea volume while it decreases with increasing the pH. Spectral reflectivity and absorption coefficient slightly depend on the film thickness probably due to an increase in the film roughness. Deposition time has a limited effect on electrical resistivity. In contrast, the pH value and thiourea volume have a large influence on resistivity and activation energy of conductivity.

References

[1] M.T.S. Nair and P.K. Nair, *Semicond. Sci. Technol.*, 13 (1998) 1164.

[2] M.C. Brelle et al., *Pure Appl. Chem.*, 72 (2000) 101.

[3] L. Isac et al., *Thin Solid Films*, 515 (2007) 5755.

[4] G.A. Alozie and F.C. Eze, *Globe J. Pure Appl. Sci.*, 9 (2003) 591.

[5] F.I. Ezema and P.E. Ugwuoke, *The Pacific J. Sci. Technol.*, 5 (2003) 33.

[6] J.G. Vazquez-Luna, A. Zehe and O. Zelaya-Angel, *Cryst. Res. Technol.*, 34 (1999) 949.

[7] I. Grozdanov, *Semicond. Sci. Technol.*, 9 (1994) 1234.

[8] P.K. Nair and M.T.S. Nair, *Solar Cells*, 22 (1987) 103.

[9] G.K. Padam and S.U.M. Rao, *Solar Energy Mater.*, 13 (1986) 297.

[10] G.K. Padam and Su. M. Rao, *Solar Energy Mater.*, 15 (1987) 227.

[11] D .Cahen, *Solar Energy Mater.*, 15 (1987) 225.

[12] K.L. Chopra, **"Thin Film Phenomena"**, McGraw-Hill Book Company.

[13] S.V. Bagul, S.D. Chavhan and R. Sharma, *J. Phys. Chem. Solids*, 68 (2007) 1623.

[14] H.M. Pathan, J.D. Desai and C.D. Lokhande, *Appl. Surf. Sci.*, 202 (2002) 47.

[15] B. Rezig, S. Duchemin and F. Guastavino, *Solar Energy Mater.*, 2 (1979) 53.

This article was reviewed at College of Materials Science and Engineering, Beijing University of Technology, CHINA, Department of Physics, University of Warsaw, POLAND, and School of Applied Sciences, University of Technology, Baghdad, IRAQ

Ali Mazahery
Mohsen Ostad Shabani

Materials and Energy
Research Center (MERC),
P.O. Box 14155-4777,
Tehran, Iran

Characterization of Commercial Al-Si Casting Alloys Reinforced with Nano SiC Composites

This paper is aimed at studying the microstructure and mechanical properties of nano composites, processed via stir casting. The composites are based on the A356 aluminum alloy, reinforced with nano-SiC particles. The density measurements showed that the samples contained little porosity, and the amount of porosity in the composites increased with increasing volume fraction. The microstructures of composites were examined using optical microscopy (OM) and transmission electron microscopy (TEM). Microscopic observations of the microstructures revealed that the dispersion of the particles was uniform. The tensile strength (yield strength and ultimate tensile strength) and the Young's modulus improve with the addition of nano particles although some reduction in ductility is observed. The highest yield strength and UTS was obtained by 3.5 vol. % of SiC nano-particles. A relatively ductile fracture in tensile fractured samples was observed by fractography examination.

Keywords: Aluminum matrix composites, Silicon carbides, Microstructure fractography, Nanostructures
Received: 15 February 2012, Revised: 23 May 2012, Accepted: 30 May 2012

1. Introduction

During the last two decades a lot of research has been conducted on aluminium matrix composites (AMCs) in commercial laboratories and small businesses. As a result of these activities, many new AMCs applications have been established, and most of these have found insertion within the commercial sector. Important AMCs applications in the aerospace and infrastructure industries have been enabled by functional properties that include high structural efficiency, excellent wear resistance, and attractive thermal and electrical characteristics. Challenging technical issues have been overcome, including compatibility between reinforcement and matrix, affordable primary and secondary processing techniques capable of adequately controlling reinforcement distribution, engineering design methodologies, and characterization and control of interfacial properties [1-8].

The recent investigations found that the incorporation of nano-particles into the aluminum matrix enhance the hardness, yield and ultimate tensile strength considerably, while the ductility is retained [9, 10]. The great enhancement in strength values of these composites was attributed to grain refinement, the strong multidirectional thermal stress at the matrix/nano particle interface, small size of nano particle, good distribution of the nano particles, and low degree of porosity which leads to effective transfer of applied tensile load to the uniformly distributed strong nano particulates. The strength of composites is expected to be influenced by the dislocation density, dislocation-to-dislocation interaction and constraint of plastic flow due to resistance offered by particles. It is reported that due to the thermal mismatch stress, there is a possibility of increased dislocation density within the matrix which lead to making local stress and also increase in strength of the matrix, and thus to the composite. More than 50% improvement in yield strength of A356 alloy was observed only with 2.0 wt. % of nano-sized SiC particles [8]. Zhao et al. [2] characterized the properties and deformation behavior of aluminum matrix nano-composites. It is reported that elongation, ultimate tensile strength and yield strength of nano-composites are enhanced with increasing of particulate volume fraction, and are markedly higher than that of Al composites synthesized by micro size particles.

This paper is aimed at the characterization of microstructure and mechanical properties in commercial Al-Si casting alloys reinforced with nano SiC composites.

2. Experiments

Due to its good castability the aluminium alloy A359, with the chemical composition listed in Table (1), was used as matrix material.

A mixture of nano-SiC and aluminum particles with respectively average particle size of 50 nm and 16 μm was used as the reinforcement. The powders were mixed in the ratio of Al/SiC=1.67 and ball milled in isopropyl alcohol for 20 min using WC/Co balls. The mixture was then dried in a rotary vacuum evaporator and passed through a 60 mesh screen. The powder mixtures were cold pressed under 200 MPa into samples having 60×60×60 mm^3 dimension. The compacted samples were crushed and then passed through 60 mesh screen. The required amount of SiC was calculated according to the ratio of Al/SiC. Aluminum 356 alloy was selected as the matrix and 1 wt. % magnesium additive in powder form was also used as a wetting agent. Experiments were carried out using a relatively simple experimental set-up which consists of several parts. The main part allows temperatures of up to 1000°C to be reached. This is surrounded by a 50 mm thick layer of kaowool insulator to minimize heat loss. Inside the heater band is a graphite crucible for holding the materials, which has a lid. Weighed quantity of Al-356 alloy was charged into the crucible and heated up to 750^oC (above the alloy liquidus temperature) for melting. There is a nitrogen supply to the crucible in order to minimize the oxidation of molten aluminum, and a graphite stirrer mounted on a graphite shaft passes through small hole out of the crucible lid. This hole also acts as the outlet for the nitrogen gas. The shaft is connected to a digital DC motor used to stir the slurry. The end of the shaft is used to facilitate bottom pouring of the composite melt. During stirring it acts as a plug at the bottom of the crucible and, for pouring, the stirring rod assembly is lifted a distance of 5–10 mm, thus opening the stopper and allowing the slurry to flow into a mould beneath the set-up. This feature is to ensure that the impurities floating on the surface of the melt are not mixed into it.

Table (1) Chemical composition of the aluminium alloy used as matrix

Element	Al	Si	Fe	Cu	Mg
Wt%	Balance	7.2	0.12	0.001	0.33
Element	Mn	Zn	Ti	Ni	
Wt%	0.02	0.02	0.01	0.04	

The powder mixture was inserted into an aluminium foil by forming a packet and added into molten metal of crucible when the vortex was formed. The packet of mixture melted and the particles started to distribute around the alloy sample.

Microstructural evaluations were carried out using optical microscope, scanning electron microscope (SEM) and transmission electron microscope (TEM). Optical microscope and SEM specimens were ground through grit papers and etched with Keller's reagent (2 ml HF (48%), 3 ml HCl (conc.), 5 ml HNO_3 (conc.) and 190 ml water). TEM specimens were machined to 0.5mm thickness and cut using a wire electro discharge machine. The samples were then ground down (350 to 1200 grit) and perforated using double spew with methanol solution. The experimental density of the composites was obtained by the Archimedian method of weighing small pieces cut from the composite cylinder first in air and then in water, while the theoretical density was calculated using the mixture rule according to the weight fraction of the nano particles. The porosities of the produced composites were evaluated from the difference between the expected and the observed density of each sample.

The tension tests were used to assess the mechanical behavior of the composites. The tensile specimens were machined from composite rods according to ASTM.B 557 standard. For each volume fraction of SiC particles, three samples were tested. In order to study the effect of nano-particles on the fracture mechanisms during tensile loading of the samples, fractography was performed on the fractured surfaces of composite specimens. To study the hardness, the Brinell hardness values of the samples were measured on the polished samples using a ball with 2.5mm diameter at a load of 31.25 kg.

3. Results and Discussions

Optical micrographs of unreinforced Al alloy and composites reinforced with SiC particles are shown in Fig. (1). Dendritic microstructure, as the result of casting process is clearly revealed in this figure. This trend was observed in previous works [9,10].

(a)

(b)

Fig. (1) Optical photomicrographs: (a) unreinforced A356 alloy (b) A356 reinforced with 1.5 vol. % SiC

Further study of these composites with high magnification bright field TEM shows the uniform distribution of SiC particles through the matrix alloy (Fig. 2). It is assumed that the uniform dispersion of nano-particles provides some heterogeneous nucleation sites during solidification, resulting in a more refined microstructure. Figure (3) shows the grain morphology results of the composites.

Fig. (2) TEM bright field image of composites with 3.5 vol.% nano-SiC particles

Energy dispersion spectrum (EDS analysis) was utilized to determine the composition of the nano-composite (Fig. 4). The detection zone of EDS beam is bigger than the average size of SiC, therefore the EDS peaks for SiC nano-paricles will inevitably include compositional information of Al matrix near particles. However, according to the compositional information of matrix, it is evident that Si and C peaks correspond to composition of nano-particles.

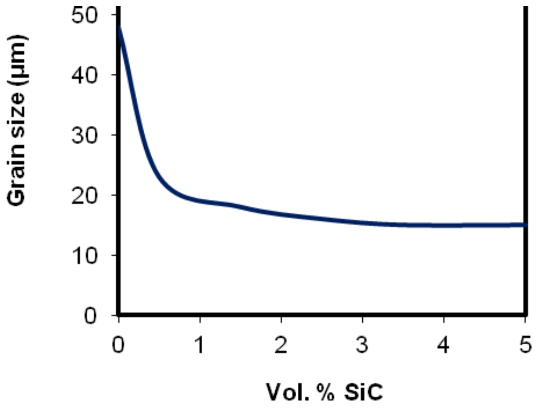

Fig. (3) Results of grain morphology

(a)

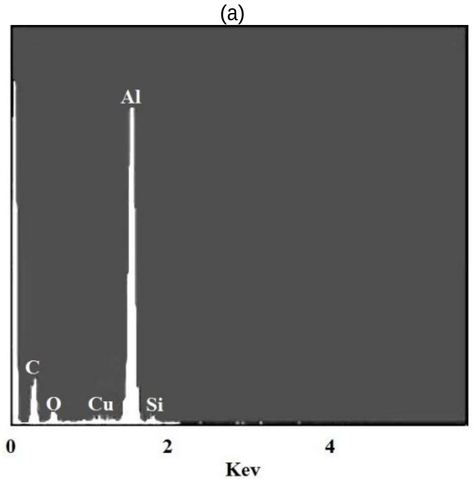

(b)

Fig. (4) (a) SEM micrograph and (b) EDS Spectrum of the sample with 2.5 vol. % SiC

Comparison of the measured density of the cast alloy and the composites with that of their theoretical density determined the amount of porosity. Figure (5) shows the variation of porosity with the volume fraction of nano-SiC particles. Higher degree of defects and micro-porosity is observed at higher SiC content which is the result of increase in the amount of interface area [11, 12].

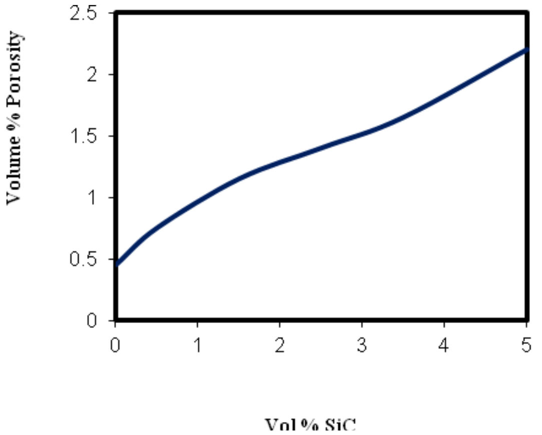

Fig. (5) Variations of porosity with the nano-SiC content

Hardness tests were performed using a Brinell hardness machine. In order to obtain the average values of hardness, areas predominant in the soft matrix or the hard reinforcing phase should be avoided so that the average values of hardness are attained from these measurements. The variation in hardness with volume fraction for Al/nano-SiC composites are summarized in Fig. (6).

Fig. (6) Variation of hardness as a function of vol.% SiC particulates

It is clear from the graph that the hardness of the composites is higher than that of the non-reinforced alloy. The higher hardness of the composites could be attributed to the fact that SiC particles act as obstacles to the motion of dislocation. The hardness increment can also be attributed to reduced grain size. As shown, hardness increases with the amount of SiC present particles. It is believed that since SiC particles are harder than aluminum alloy, their inherent property of hardness is rendered to the soft matrix [13, 14].

Figures (7), (8) and (9) display the tensile flow curves, yield strength and UTS of the composites, respectively.

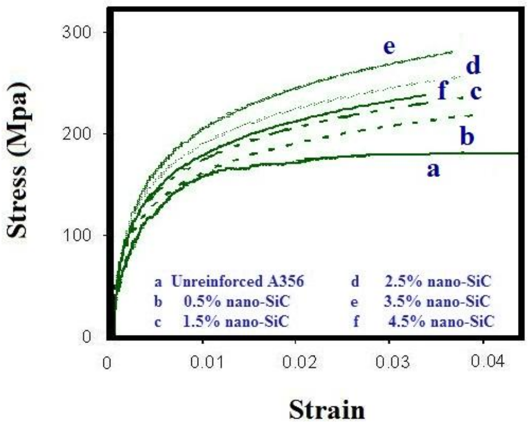

Fig. (7) Flow curves in tensile deformation of the composites

It could be noted that the flow curves do not show any sharp yield point irrespective of the material and the strength values increases with the addition of nano-SiC particles. It is believed that the great enhancement in tensile flow stress observed in these composites is due to good distribution of the nano-SiC particles and low degree of porosity which leads to effective transfer of applied tensile load to the uniformly distributed strong SiC particulates. The grain refinement and strong multidirectional thermal stress at the Al/SiC interface are also important factors, which play a significant role in the high strength of the composites. SiC particles have grain-refined strengthening effect, since they act as the heterogeneous nucleation catalyst for aluminum which is improved with increase in the volume fraction [9-15].

Fig. (8) Variations of yield strength as a function of vol. % nano-SiC particulates

Fig. (9) Variations of UTS as a function of vol. % nano-SiC particulates

The difference between the coefficient of thermal expansion (CTE) values of matrix and ceramic particles generates thermally induced residual stresses and increase dislocations density upon rapid solidification during the fabrication process. The interaction of dislocations with the non-shearable nano-particles increases the strength level of composite samples. According to the Orowan mechanism, the nano-SiC particles act as obstacles to hinder the motion of dislocations near the particles in the matrix. This effect of particles on the matrix is enhanced gradually with the increase of particulate volume fraction [2, 10].

According to the results of this experiment, quite significant improvement in strength is noted initially when particles are added; however, further increase in SiC content leads to reduction in strength values. The weakening factors of mechanical properties might be responsible for this including particles clusters and porosity. Hereby, it is believed that strengthening and weakening factors of mechanical properties could neutralize the effect of each other and thus, the composite containing 3.5 vol. % SiC exhibits maximum tensile flow stress. Normally micron-sized particles are used to improve the ultimate tensile and the yield strengths of the metal. However, the ductility of the MMCs deteriorates significantly with high ceramic particle concentration [16-18].

It is of interest to use nano-sized ceramic particles to strengthen the metal matrix, while maintaining good ductility [6,19]. It is inferred from Fig. (10) that the addition nano-particles deteriorate the ductility of A356 alloy. The stir casting method that is used in the present work to produce the nano-composites can most probably create different interfaces between nano-particles and matrices and thus, encourage crack initiation and propagation [10]. It is also noted that the elongation remain rather constant with the addition of nano particles. This is consistent with the findings of Hassan and Gupta [20, 21].

Fig. (10) Variations of elongation as a function of vol. % nano-SiC particulates

Fig. (11) SEM fractograph of tensile fracture surface for the composites with 3.5 vol. % nano-SiC particles

Typical SEM micrographs of tensile fracture surfaces for composites are shown in Fig. (9). The tensile fracture surfaces of the samples are clearly indicative of lot of dispersed shallow and small dimples with varying sizes in the matrix, confirming the high ductility observed in the tensile studies. However, there are a number of larger dimples linked together along the boundaries, showing increased degree of clustering along the grain boundaries (Fig. 11).

4. Conclusions

In this research, nano-sized SiC particles were successfully incorporated into the aluminum matrix. Optical microscope examination revealed the grain refining effect of nano-particles. A reasonably uniform distribution of SiC nano-particles in the Al matrix was observed by electron microscopes. Porosity level increased slightly with increasing particulate content which can be attributed to the increased surface area of the nano-SiC particles. The addition of nano-particles resulted in significant improvements in hardness, yield strength and UTS of the composites. Different strengthening mechanisms contributed in the obtained strength improvements including Orowan strengthening, grain refinement, accommodation of CTE mismatch between the matrix and the particles, and the load bearing effects. The dispersed dimples with varying sizes were observed in the fractured surface tensile specimens, confirming the high ductility of the nano-composites.

References

[1] Tu J.P. et al., *Mater Lett*., 2002; 52(6): 448–452.

[2] Zhao Y.T. et al., *Compos. Sci. Technol*., 2008; 68: 1463–1470.

[3] Shabani M.O. and A. Mazahery, *Synthetic Metals*; 161 (2011) 1226–1231.

[4] Ferkel H. and B.L. Mordike, *Mater. Sci. Eng.* A 2001; 298: 193–199.

[5] Akio K. et al., *J. Jpn. Inst. Light Met.* 1999; 49: 149–154.

[6] Shabani M.O. and A. Mazahery, *J. Mater. Sci.*, (2011) 46:6700–6708.

[7] Lan J., Y. Yang and X. Li, *Mater. Sci. Eng.* A 2004; 386: 284–290.

[8] Lan J., Y. Yang and X. Li X, *Mater. Sci. Eng.* A 2004; 380: 378–383.

[9] Mazahery A., H. Abdizadeh and H.R. Baharvandi, *Mater. Sci. Eng*. A 2009; 518: 61–64.

[10] Habibnejad-Korayema M., R. Mahmudia and W.J. Pooleb, *Mater. Sci. Eng.* A 2009;

[11] Suresh K.R. et al., Proc. of the 14th Int. Conf. on Wear of Materials, August–September, 2003, 638.

[12] Hassan S.F. and M. Gupta, *Metallurg. Mater. Trans.*, 2005; 36A: 2253–2258.

[13] Cooke P.S. and P.S. Werner, *Mater. Sci. Eng.* A144 (1991) 189–193.

[14] Mondal D.P., N.V. Ganesh and V.S. Muneshwar, *Mater. Sci. Eng.* 2006; 433: 18–31.

[15] Watson M.C. and T.W. Cline, *Acta Metallurg. Mater.*, 1992; 40: 131–139.

[16] Reddy R.G., *Rev. Adv. Mater. Sci.*, 2003; 5: 121–133.
[17] Kang Y.C. and S.L.I. Chen, *Mater. Chem. Phys.,* 2004; 85(2–3): 438–443.
[18] Hirata Y. et al., *J. Euro. Ceram. Soc.*, 30(9), 2010, 1945-1954.
[19] Mussert K.M. et al., *J. Mater. Sci.*, 2002; 37: 789–794.
[20] Hassan S.F. and Gupta M., *J. Mater. Sci.*, 2006; 41: 2229–2236.
[21] Hassan S.F. and Gupta M., *Mater. Sci. Eng.* A 2005; 392: 163–168.

Phase Noise Compensation for Coherent Orthogonal Frequency Division Multiplexing in Optical Fiber Communications Systems

Jassim K. Hmood

Department of Laser and
Optoelectronics Engineering,
University of Technology,
Baghdad, Iraq
jassim_711@yahoo.com

In this paper, the Coherent Optical (CO) systems using Orthogonal Frequency Division Multiplexing (OFDM) for dispersion compensation is demonstrated. The Quadrature Amplitude Modulation QAM-OFDM transmitter signal was controlled by the Mach-Zender Modulator (MZM) which modulates the laser source with wavelength of 1550nm. The heterodyne receiver with dual-polarization optoelectronic down-converter is used to obtain good coherent detection without using optical phase locked loop. The analytical part was done using a software simulator. All the proposed system components were simulated using VPIphotonic simulation software for testing CO-OFDM system. The transmitted signal, optical spectrum, eye diagram and constellation diagram was obtained to evaluate system performance.

Keywords: Optical fibers, OFDM, Coherent communications, Heterodyne
Received: 26 March 2009, **Revised**: 3 May 2009, **Accepted**: 10 May 2009

1. Introduction

Orthogonal frequency-division multiplexing (OFDM) is a multi-carrier technique that has been deployed in optical fiber communications. A multi-carrier system sends information over N-frequency-division-multiplexed (FDM) channels, each modulated by a different carrier. The total bit rate of the OFDM stream is the sum of bit rates in all narrowband channels. These narrowband channels are also called tones and OFDM is also called multi-tone modulation. Each tone in OFDM can use a different modulation inside it, for example, BPSK, QPSK, and QAM [1]. Coherent optical OFDM (CO-OFDM) has been proposed to combat fiber chromatic and polarization-mode dispersion [2]. Therefore, it can be used to compensate for fiber chromatic dispersion in ultra-long haul communications links [3]. Also, it shows that the CO-OFDM system could provide a feasible solution to the mitigation of Polarization Mode Dispersion (PMD) in existing installed fiber links [4,5].

The simulation was done by an advanced optical communications system simulation package designed for professional engineering called VPIphotonics simulating software by VPIsystems. VPIphotonics, represents an optical communications system as an interconnected set of blocks. Each block is simulated independently using the parameters specified by the user for that block and the signal information passed into it from other blocks [6].

This paper discusses coherent optical OFDM communications system, gives overview on coherent detection and shows that detection without using optical or electrical Phase Locked Loop (PLL) is possible. As well, details of proposed communications system are explained and explanation of simulation of CO-OFDM system and some simulation results of the CO-OFDM system are presented.

2. Coherent Detection

The most advanced detection method is coherent detection, where the receiver computes decision variables based on the recovery of the full electric field, which contains both amplitude and phase information. Coherent detection thus allows the greatest flexibility in modulation formats, as information can be encoded in amplitude and phase, or alternatively in both in-phase (I) and quadrature (Q) components of a carrier. At the receiving end, the receiver first adds a locally generated optical wave to the incoming information-bearing signal and then detects the combination. Coherent detection requires the receiver to have knowledge of the carrier phase, as the received signal is demodulated by a local oscillator (LO) that serves as an absolute phase reference. There are two basic demodulation formats, depending on how the signal is mixed with the local oscillator which gives heterodyne or homodyne detection [7].

The received signal is detected either synchronously or asynchronously. The synchronous detection is more sensitive than asynchronous detection therefore it used in good coherent optical detection. Traditionally, carrier synchronization has been performed by a phase-locked loop (PLL). Optical systems can use one of the following ways:

(i) An optical PLL (OPLL) that synchronizes the frequency and phase of the LO laser with the TX laser.

(ii) An electrical PLL where down-conversion using a free-running LO laser is followed by a second stage demodulation by an analog or digital electrical VCO whose frequency and phase are synchronized.

PLL's are sensitive to propagation delay in the feedback path, and the delay requirement can be difficult to satisfy. The principle of polarization insensitivity for CO-OFDM system use Feed-forward (FF) carrier synchronization overcomes the propagation delay problem [4]. In addition, as a FF synchronizer uses both past and future symbols to estimate the carrier phase, it can achieve better performance than a PLL which, as a feedback system, can only employ past symbols.

3. CO-OFDM Transmission System

A coherent CO-OFDM transmission system is shown in Fig. (1). At the transmitter, the OFDM symbol is generated as follows: NQAM input QAM symbols are zero-padded to obtain NFFT input samples for inverse FFT (IFFT), NG non-zero samples are inserted to create the guard interval, and the OFDM symbol is multiplied by the window function [8]. Two Mach- Zehnder modulators (MZMs) encode the RF OFDM signal onto an optical carrier and perform pulse shaping. Two MZMs are needed, one for each polarization (I and Q). The laser diode output is used as a CW source is split into two orthogonal polarization components, which are modulated separately and combined in a polarization beam splitter (PBS). Also, it can be added modulation format (e. g. NRZ or RZ) to the optical signal for increase the sensitivity of receiver.

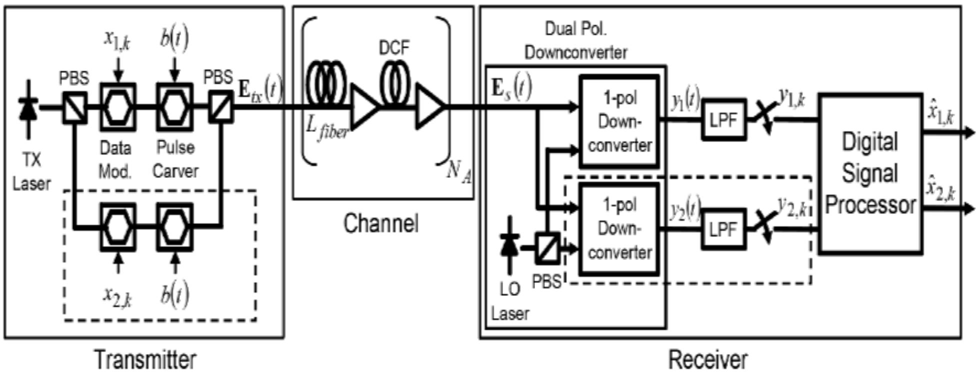

Fig. (1) Coherent transmission system

The first stage of a coherent receiver is a dual-polarization optoelectronic down-converter that recovers the base-band modulated signal. A dual-polarization down-converter is shown inside the receiver of Fig. (1). The output of a local oscillator laser must be added to the received signal with an identical polarization before photo-detection; alternatively, a polarization diversity receiver can be used [9]. The local oscillator (LO) laser is polarized at 45° relative to the polarized beam split (PBS), and the received signal is separately demodulated by each LO component using two single-polarization down-converters in parallel. The four outputs are the I and Q of the two polarizations, which has the full information of electrical field of optical signal at end of fiber $E_s(t)$.

A single-polarization down-converter, involve the LO laser is aligned in the certain polarization. Down-conversion from optical pass-band to electrical base-band can be achieved either by a homodyne or by a heterodyne receiver. In case of the heterodyne receiver, the local oscillator and transmitter (TX) lasers differ by an intermediate frequency (IF), and an electrical LO is used to down-convert the IF signal to base-band.

4. Simulation Analysis for CO-OFD System

The experiment setup is illustrated in Fig. (2). This system is simulated by using VPIphotonic simulation software. The experimental setup of CO-OFDM system uses direct up/down conversion architecture and intermediate frequency (IF) architecture. This setup can operate either on direct up/down conversion architecture or direct up/IF down-conversion architecture by select the analog switch in clock either to clock recovery or to electrical local oscillator.

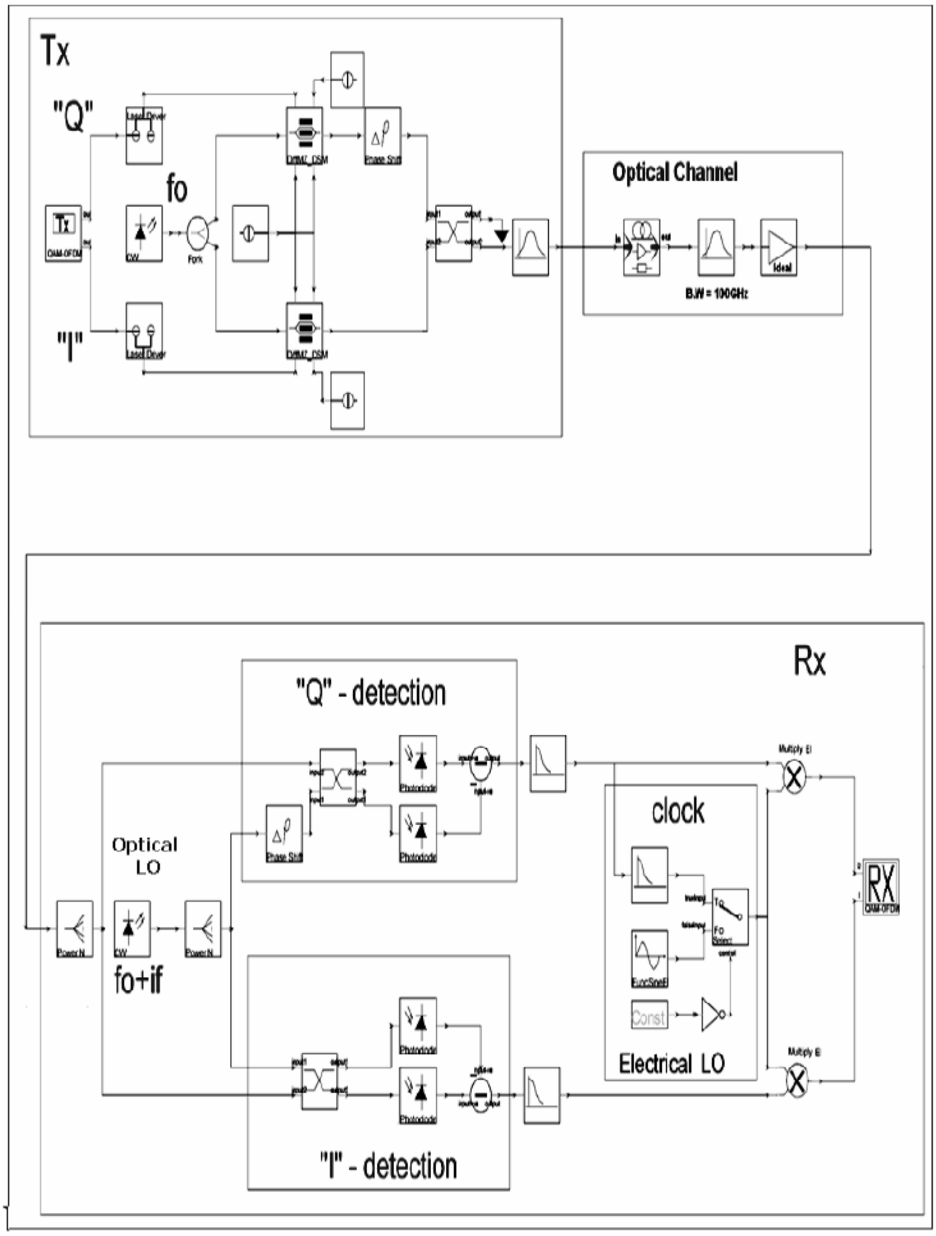

Fig. (2) The experiment setup of CO-OFDM communication system

In the direct up-conversion architecture, the optical transmitter consists of QAM-OFDM transmitter with I and Q signals and modulation format of NRZ, CW laser with optical frequency (f_o) as optical source, two Mach-Zender modulators (MZM's) to up-convert the real/imaginary parts of the QAM-OFDM transmitter, from the RF domain to the optical domain, i.e., each MZM is respectively driven by the real or imaginary part of the transmitter signal, and fiber couplers to recombine outputs of two MZM's and lunched to the optical channel.

The carver is not shown in OFDM system because it represents pulse shape or modulation format (e.g, NRZ or RZ). In this simulation, the modulation format is set inside TX of (QAM-OFDM) to NRZ modulation format. The transmitted signal can be written as:

$$E_{tx}(t) = \begin{bmatrix} E_{tx,1}(t) \\ E_{tx,2}(t) \end{bmatrix} = \sqrt{P_t}\sum_k x_k b(t-kT_s)e^{j(\omega_s t+\phi_s(t))} \qquad (1)$$

where T_s is the symbol period, P_t is the average transmitted power, $b(t)$ is the pulse shape (e.g., non-return-to-zero (NRZ) or return-to-zero (RZ)), ω_s and $\phi_s(t)$ are the frequency and phase noise of the TX laser, and $x_k=[x_{1,2},x_{2,k}]^T$ is a 2×1 complex vector representing the *k*-th transmitted symbol.

In the direct down-conversion (homodyne) architecture, the OFDM optical receiver involves dual-polarization optoelectronic down-converter uses two pairs of balanced receivers and an optical 90° hybrid to perform optical I/Q detection. The RF OFDM receiver performs OFDM base-band processing to recover the data. The advantages for such direct-conversion architecture are (i) no need for image rejection filter in both transmitter and receiver, and (ii) significant reduction of the required electrical bandwidth for both transmitter and receiver [10].

In the IF down-conversion system (heterodyne), the optical OFDM signal is first down-converted to an intermediate frequency IF and the electrical I/Q detection is performed. The heterodyne receiver involves dual-polarization optoelectronic down-converter, CW local oscillator laser running with optical frequency (f_o +IF), electric LO used for down-conversion of the IF signal to base band. In a coherent receiver, a local oscillator (LO) is required to down-convert the received signal. In general, the LO will have random phase fluctuations relative to the transmitter oscillator. The distortion due to transmitter laser and receiver LO phase noise will then appear as a random rotation of points in the received constellation [11].

Optical channel involves the optical fiber and optical amplifier. Optical signal-to-noise ratio (OSNR) can be set from 20dB to 50dB by adding amplifier spontaneous emitting (ASE) noise to the optical signal.

Zero-padding encoding is used to generate the OFDM signal, so that the clock signal and modulated signal do not overlap in frequency as shown in Fig. (3). It was shown that in the noiseless case with ZP-OFDM, the transmit symbol can be recovered regardless of the channel zero locations [12].

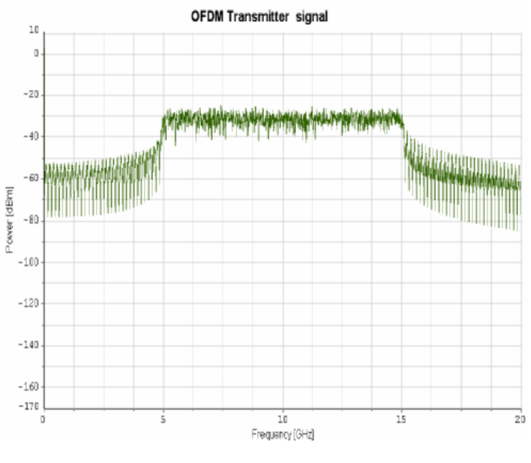

Fig. (3) Zero-padding OFDM transmitter signal

One of the parameters governing performance is the laser source linewidth. For different laser and LO linewidth (LW) values (10^5, 10^6 and 10^7) Hz, clock (eye diagram of receive signal) can be observed as shown in Fig. (4). The influence of laser and LO linewidth on the received constellation diagram is shown in Fig. (5). This test was performed under OSNR of 35dB and laser driver bias of 0.03.

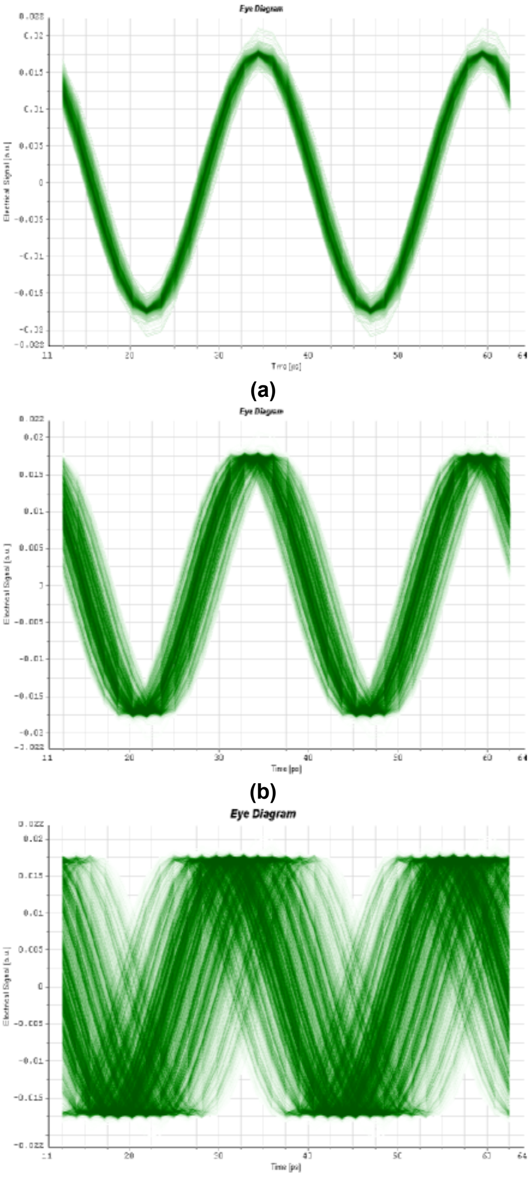

(a)

(b)

(c)

Fig. (4) The Influence of laser linewidth on the received eye diagram (a) LW=10^5Hz, (b) LW=10^6Hz, (c) LW=10^7Hz

The clock information (phase and frequency mismatch between transmitter and receiver) is contained in the "laser LO" beat term that is extracted at the receiver using an electrical filter and used for down-conversion and phase correction.

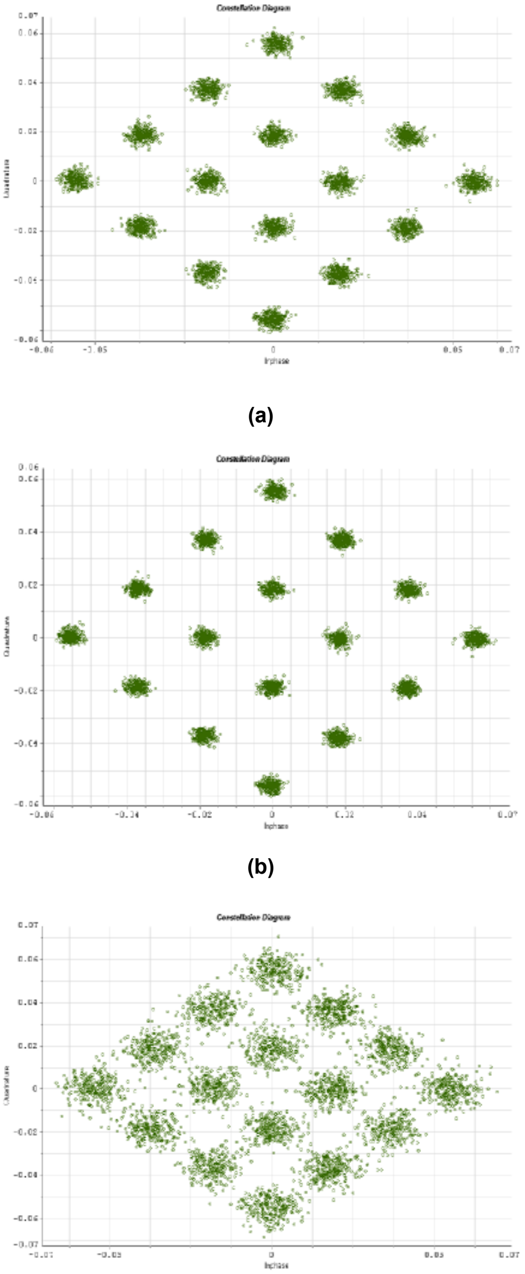

(a)

(b)

(c)

Fig. (5) The influence of laser and LO linewidth on the received constellation diagram (a) LW=10^5Hz, (b) LW=10^6Hz, (c) LW=10^7Hz

The performance of the proposed method depends on the strength of the extracted clock signal, which can be tuned by dividing the In-phase (I) and Quadrature (Q) MZM's slightly asymmetrical, i.e., the MZM is slightly biased. Therefore, the eye-diagram and the constellation diagram are the best with bias of 0.05V and they become worst with bias of 0 and 0.1V, as shown in Fig. (6).

The optical ASE noise is modeled as white Gaussian noise, and laser phase noise is assumed to be white frequency noise. The influence of phase noise in OFDM systems is two-fold, i.e., it generates a common phase rotation of all the sub-carriers in one symbol and a cross-leakage between the sub-carriers named inter-carrier interference (ICI).

The receiver performance of CO-OFDM system with influence of noise is shown in Fig. (7), in which, the experiment system is tested with OSNR of 20dB, 35dB and 50dB, respectively. The effect of OSNR on the optical spectrum, constellation diagram and clock signal is plotted. The influence increasing of OSNR on the received optical spectrum is making the noise level under -47dB. Also, the constellation diagram becomes clearer with increasing OSNR because the strength of the extracted clock signal becomes high. Figure (8) illustrates the relation between the BER and the laser source linewidth at OSNR of 25dB and 35dB. For OSNR of 25dB, lower BER (10^{-5}) at laser linewidth of 10kHz. The BER increased slightly for linewidth of 100kHz and it became very high with 10MHz and the system failed to detect optical signal. For OSNR of 35dB, lower BER of $2x10^{-6}$ at laser linewidth of 10kHz. The BER increased slightly for linewidth of 100kHz and reached to 10^{-4} for linewidth of 10MHz and the system still at suitable operation.

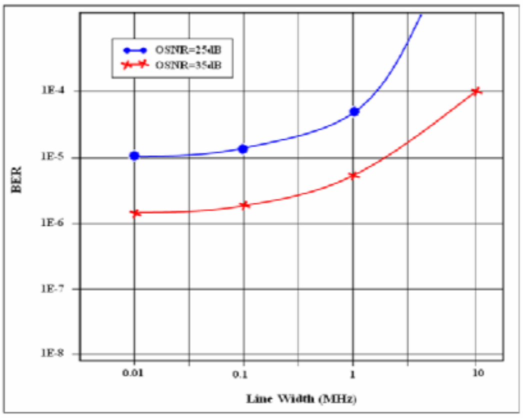

Fig. (8) Relation of laser source linewidth with BER at different OSNR

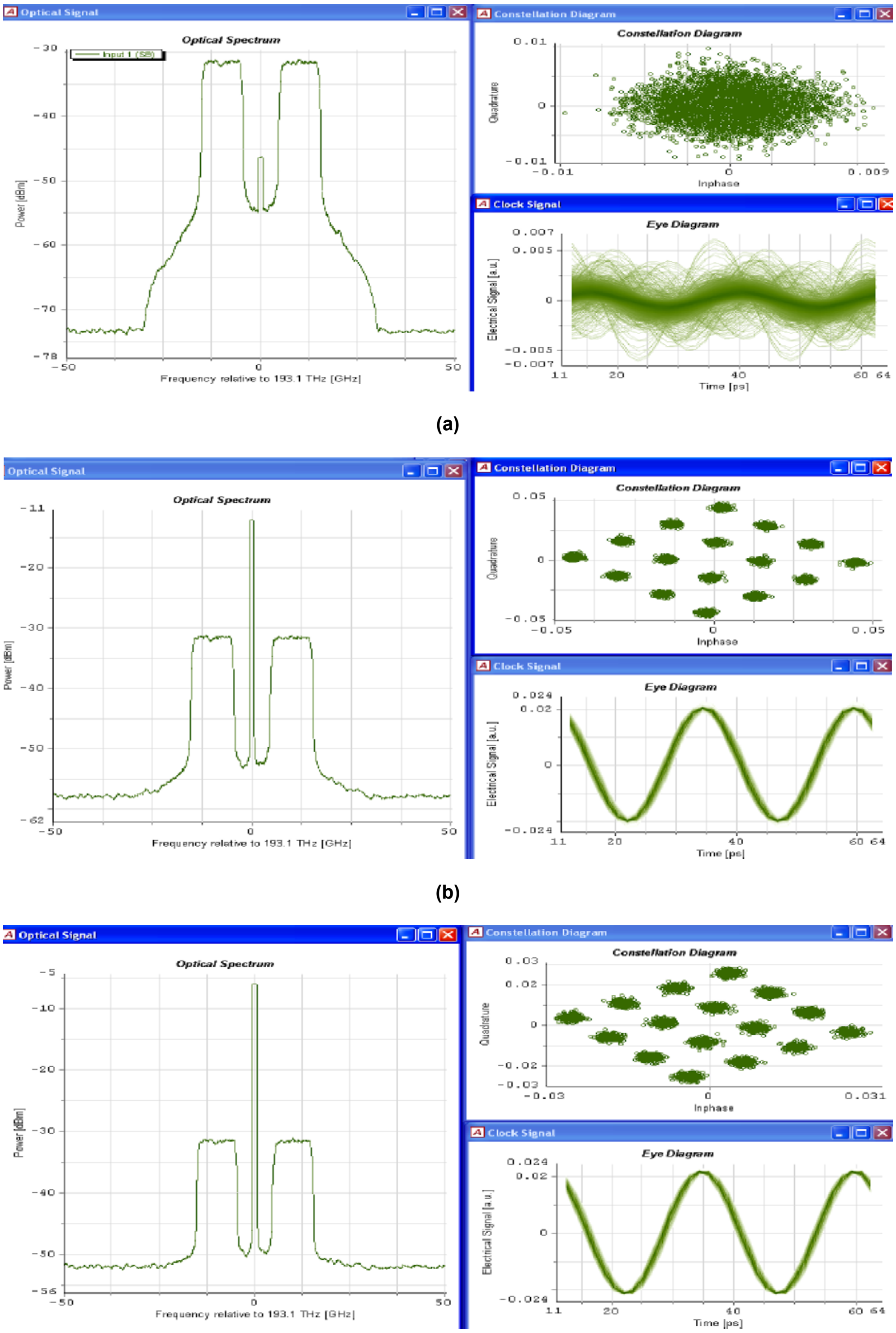

(a)

(b)

(c)

Fig. (6) The effect of changing MZM bias on the receiver performance at bias of (a) 0, (b) 0.05V, and (c) 0.1V

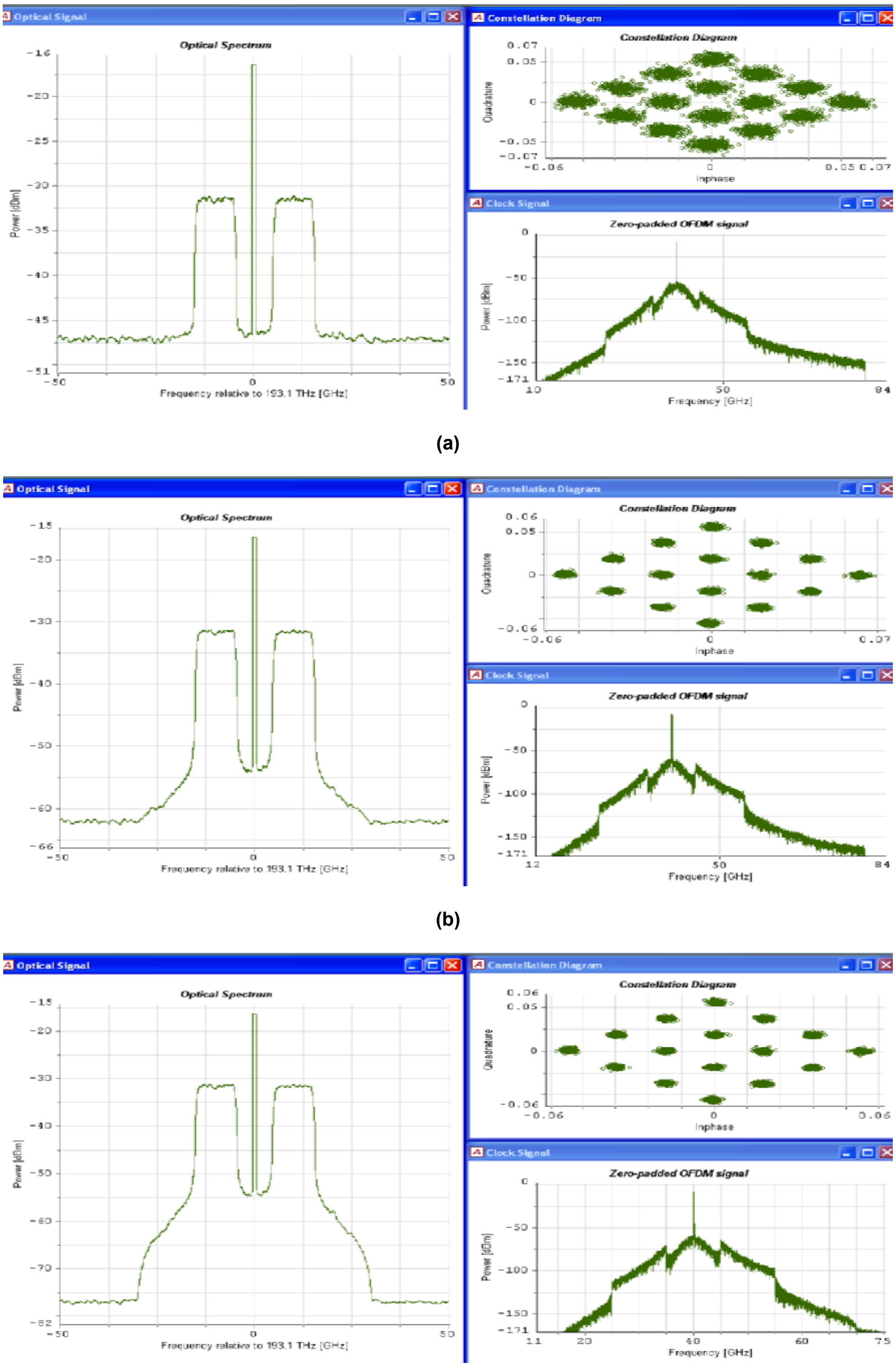

(a)

(b)

(c)

Fig. (7) The influence of noise on the optical spectrum, received spectrum and constellation diagram at OSNR of (a) 20dB, (b) 35dB, and (c) 50dB

5. Conclusion

This paper reports and depicts the results of using CO-OFDM telecommunications system in high bit rate optical transmission systems. The drive for higher performance in optical fiber systems can be achieved by coherent detection. The dual-polarization heterodyne down-conversion is linear process that can fully recover the received signal field. The coherent heterodyne detection of high bit rate OFDM signals without electric or optical-locked loop (PLL) was studied. The analytical study was employing standard optical fibers. The laser linewidth had an effect on the optical communications system; therefore, the laser linewidth must be set to approximately 10^6Hz for suitable performance. The suitable system performance obtained by slightly tuning I and Q MZM's to bias of 0.05V.

References

[1] A. Ahmad, **"Wireless and Mobile Data Networks"**, John Wiley & Sons, Inc. (2005), Ch.4, 76.
[2] W. Shieh and C. Athaudage, *IEE Proc. Electron. Lett.*, 42 (2006) 587-588.
[3] A.J. Lowery and J. Armstrong, *Optics Express*, 14(6) (2006) 2079-2084.
[4] W. Shieh, W. Chen and R.S. Tucker, *IEE Proc. Electron. Lett.*, 42 (2006) 996-997.
[5] S.L. Jansen et al., "Optical OFDM - A Candidate for Future Long-Haul Optical Transmission Systems", Optical Fiber communication/National Fiber Optic Engineers Conference, 2008. OFC/NFOEC 2008, 24-28 Feb. (2008) 1-3.
[6] VPIsystems Inc. "Photonic Design Automation, Expert Solutions for Optical Equipment Design".
[7] G. Keiser, **"Optical Fiber Communications"**, 2nd ed., McGraw-Hill (1991) 379-380.
[8] I.B. Djordjevic, L. Xu, and T. Wang, *Optics Express*, 16(19) (2008) 14845-14852.
[9] W. Shieh, H. Bao, and Y. Tang, "Coherent optical OFDM: theory and design", *Optics Express*, 16(2) (2008) 841-859.
[10] A.J. Lowery, S. Wang and M. Premaratne, *Optics Express*, 15(20) (2007) 13282-13287.
[11] A.H. Sayed et al., *Lightwave Technol.*, 24(3) (2006) 1269-1276.
[12] S. Pfletschinger and F. Sanzi, "Iterative Demapping for OFDM with Zero Padding or Cyclic Prefix", IEEE Int. Conf. on Communication (ICC), Paris (2004), 842-846.

MNC 2009

22nd International Microprocesses and Nanotechnology Conference

November 16-19, 2009

Conference Site:
Sheraton Sapporo Hotel, Sapporo, Japan

MNC 2009 SCOPE and SYMPOSIUM
1-1: DUV, EUV Lithography and Metrology
1-2: Electron- and Ion-Beam Lithography
1-3: Resist Materials and Processing
2-1: Nanodevices
2-2: Nanofabrication
2-3: Nanomaterials
2-4: Nano-Tool
3: Nanoimprint, Nanoprint and Rising Lithography
4: Bio MEMS, Lab on a Chip
5: Microsystem Technology and MEMS
Symposium A. Computational Lithography
Symosium B. Graphene: Growth & Characterization
Sponsored by
The Japan Applied Physics Physics

Committee Chairs:
Organizing Committee Chair:
S. Shoji (Waseda Univ.)
Steering Committee Chair:
T. Itani (Selete)
Program Committee Chari:
T. Meguro (Tokyo Univ. of Sci.)

Sponsored by
The Japan Society of Applied Physics

Cooperation
Association of Super-Advanced Electronics Technologies
The Institute of Electrical Engineers of Japan
The Institute of Electronics, Information and Communication Engineers
The Japan Society for Precision Engineering
The Japanese Society for Synchrotron Radiation Research
The Japanese Society of Electron Microscopy
The Surface Science Society of Japan
The Vacuum Society of Japan

MNC 2009 SCOPE and SYMPOSIUM

1-1:DUV, EUV Lithography and Metrology
This session focuses on DUV, EUV, Immersion Lithography, and Computational Lithography including OPC, SMO, DFM. In addition, Metrology such as SEM and Scatterometry is included.

1-2:Electron- and Ion-Beam Lithography
Electron and ion beam technologies such as lithography, metrology, inspection and repair tools. Other related technologies using charged particle beams are also welcome.

1-3:Resist Materials and Processing
Resist materials(EUV, immersion, double patterning,

Iraqi J. of Appl. Phys. , Vol. 2 , No. 1-2 , 2006 , 31-36

Alaa B. Kadhem
Ehsan M. Raheem

Ministry of Science and Technology, Applied Physics Research Center, Baghdad, IRAQ

Calculation of Charge Density Distribution of (2s-1d) Shell-Model Nuclei Using the Occupation Numbers of States

The charge density distribution (CDD) of ^{24}Mg, ^{28}Si, ^{30}Si, ^{32}S and ^{34}S nuclei have been calculated using the wave functions of the harmonic oscillator on the assumption that the occupation numbers of the states in real nuclei differ from the predictions of the simple shell model. The difference of the CDD of (^{28}Si-^{30}Si) and (^{32}S-^{34}S) isotopes have been calculated to clarify the influence of the additional neutrons on the CDD. The elastic electron scattering form factors of the considered nuclei have been calculated using the ground state charge density distributions.

Introducing an additional parameter (α) that reflects the difference of the occupation numbers of states between the real states of the nuclei and the simple shell model predictions, leads to a very good agreement between the calculated and experimental results of the CDD and form factors. This leads to the conclusion that proposing (α) as an additional parameter is a real one.

Keywords: *Electrostatic lenses, Ion-optical system, Spherical aberration, Chromatic aberration*

Received: 26 March 2006, Revised: 12 June 2006, Accepted: 25 June 2006

1. Introduction

The charge density distribution (CDD) is a fundamental characteristic of the nucleus in its ground states, and elastic electron scattering is a unique method of determination of this quantity. Here, the larger the momentum-transfer to the nucleus the more accurate is the CDD extracted from such experiment.

Various theoretical methods are used for calculations of the CDD, among them the Hartree-Fock (HF) method with Skyrme effective interaction [1,2], the theory of finite Fermi systems (TFFS) [3,4] and the single particle potential (SPP) method [5]. In the Hartree-Fock in addition to the Skyrme forces SI–SVI, the multiparametric forces Ska, Skb, ST, SM and SM* with up to ten parameters [6] are used. In the HF method the energy dependence of the effective interaction is not taken into account. Taking into account retardation effects in the TFFS improves the description of entire set of data in comparison with the HF method with effective forces [4]. However, the TFFS describes properties of medium and heavy nuclei and is inapplicable to light nuclei. In the SPP method [5] instead of the wave function of the nucleus one introduced the single particle density matrix n^1 containing complete information on the single particle properties of the nucleus. The method is close to the HF method, but here fractional filling numbers of the state n_α, which are determined from experiment, are introduced.

2. The Theory

2.1 Charge Density Distributions

The charge density distribution CDD of the shell nuclei can be evaluated by means of the wave functions of a harmonic oscillator, since [7]:

$$\rho(r) = \frac{1}{4\pi}\sum_{nl}(2j+1)R_{nl}^2(r) \tag{1}$$

where $R_{nl}(r)$ is the radial part of the harmonic oscillator wave function, which is given by [8]:

$$\begin{aligned} R_{nl}^2(r) &= [(\pi^{1/2}b^3).\{(2l+1)!!\}^2.(n-1)!]^{-1}.2^{l-n+3}.(2l+2n-1)!!.(\frac{r}{b})^{2l} \\ &* \sum_{k=0}^{n-1}[(-1)^k.\{(n-1-k)!k!(2k+2l+1)!!\}^{-1}.2^k.(n-1)!(2l+1)!!(\frac{r}{b})^{2k}]^2 * \exp(-r^2/b^2) \end{aligned} \tag{2}$$

Putting Eq. (2) into Eq. (1), in the simple shell model, the CDD for 2s-1d shell nuclei are:

$$\rho(r)=\frac{1}{\pi^{3/2}b^3}\{5+(\frac{4}{15}Z-\frac{4}{3})(\frac{r}{b})^4\}.\exp(-r^2/b^2) \quad (3)$$

where Z is the charge of the nucleus and b is the oscillator parameter.

Eq. (3) gives the CDD of 2s-1d shell nuclei on the bases of the simple shell model.

The mean square radii (MSR) of the considered nuclei are obtained according to the following equation [9]:

$$\langle r^2\rangle=\frac{4\pi}{Z}\int_0^\infty \rho(r)\,r^4\,dr \quad (4)$$

The normalization of the CDD is given by [10]:

$$Z=4\pi\int_0^\infty \rho(r)\,r^2\,dr \quad (5)$$

Substituting the form of the CDD of eq.(3) into eq.(4), we obtain the (MSR) of 2s-1d shell nuclei:

$$\langle r^2\rangle=\frac{b^2}{2}[7-\frac{20}{Z}] \quad (6)$$

In the present work, the CDD of the 2s-1d shell nuclei are calculated by means of the harmonic oscillator wave functions on assumption that filling numbers of the states in real nuclei differ from the predictions of the simplest shell-model. These numbers can be determined from the comparison between the calculated and the experimental charge density distribution. Therefore, with this assumption, the CDD for 2s-1d shell nuclei are:

$$\rho(r)=\frac{1}{\pi^{3/2}b^3}\{5-\frac{3}{2}\alpha+2\alpha(\frac{r}{b})^2+(\frac{4}{15}Z-\frac{4}{3}-\frac{2}{5}\alpha_1-\frac{2}{3}(\alpha-\alpha_1))(\frac{r}{b})^4+\frac{8}{105}(\alpha-\alpha_1)(\frac{r}{b})^6\}.\exp(-r^2/b^2) \quad (7)$$

where the parameter α which is equal to $\alpha_1+\alpha_2$ characterizes the deviation of filling numbers from the predictions of the shell-model. The CDD of Eq. (7) is obtained on the assumption that there is a core of filled 1s and 1p shells, and the proton numbers in 2s,1d and 1f shells are equal to, respectively, 2-α, Z-10+α and α_2 (in real nucleus) instead of 2, Z-10 and zero (as in the simple shell model of Eq. (3)), where the parameters α, α_1 and α_2 represent the deviation of the shell charges of 2s, 1d and 1f from the prediction of the simple shell model. The parameter α is determined from the central CDD, ρ(r=0), of Eq. (7), i.e.,

$$\rho(0)=\frac{1}{\pi^{3/2}b^3}(5-\frac{3}{2}\alpha) \quad (8)$$

Since the values of $\rho(0)$ are known, i.e., they can be taken from experiments. The harmonic oscillator size parameter b are obtained by introducing the experimental MSR of considered nuclei into Eq. (6). The parameters α_1 and α_2 are determined by:

$$\alpha_1=\frac{2}{3}(5-\pi^{3/2}b^3\rho(0))-\frac{Z}{b^2}\langle r^2\rangle-10+\frac{7}{2}Z \quad (9)$$

$$\alpha_2=\frac{Z}{b^2}\langle r^2\rangle+10-\frac{7}{2}Z \quad (10)$$

2.2 Elastic Electron Scattering Form Factors

The elastic electron scattering form factors from spin zero nuclei can be determined by the ground-state charge density distributions. In Plane Wave Born Approximation (PWBA), the incident and scattered electron waves are considered as plane waves and although this seems to be somewhat reasonable, an accurate testing of the experimental cross section values and other observable leads to the realization that using PWBA provides mainly qualitative description even for light nuclei [11,12]. Therefore, in PWBA and if the CDD is real and spherical symmetric, the form factor is simply the Fourier transform of the CDD and it is real and spherical symmetric, and vice versa [13,14]. Thus:

$$F(q)=\frac{4\pi}{Z}\int_0^\infty \rho(r)\,j_0(qr).r^2\,dr \quad (11)$$

where $j_0(qr)=\sin(qr)/dr$ is the zeroth-order spherical Bessel function and q is the momentum transfer from the incident electron to the target nucleus. Eq. (11) may be expressed as:

$$F(q)=\frac{4\pi}{qZ}\int_0^\infty \rho(r)\sin(qr)\,r\,dr \quad (12)$$

The form factors of the 2s-1d shell nuclei in the simple shell model (i.e. α=0) can be obtained by introducing the form of the CDD of Eq. (3) into Eq. (12), i.e.,

$$F(q)=\frac{1}{Z}\{Z+\frac{1}{3}(5-Z)q^2b^2+$$

$$\frac{1}{12}(\frac{Z}{5}-1)q^4b^4\}.\exp(-\frac{q^2b^2}{4}) \quad (13)$$

Similarly, the form factors of the above nuclei according to our assumption (i.e., $\alpha\neq0$) can be obtained by introducing the CDD of Eq. (7) into Eq. (12), i.e.,

$$F(q)=\frac{1}{Z}\{Z+(\frac{5}{3}-\frac{Z}{3}-\frac{1}{6}\alpha+\frac{1}{6}\alpha_1)q^2b^2+(\frac{Z}{60}-\frac{1}{12}+\frac{1}{120}\alpha-\frac{1}{30}\alpha_1)q^4b^4-[\frac{(\alpha-\alpha_1)}{840}]q^6b^6\}.\exp(-\frac{q^2b^2}{4}) \quad (14)$$

3. Results and Discussion

The calculated CDD of ^{28}Si, ^{30}Si, ^{32}S and ^{34}S nuclei have been compared with the fitted to the experimental data of Model-Independent (MI) CDD [9],while the calculated CDD of ^{24}Mg nucleus has been compared with the fitted to the experimental data of tow Parameter Fermi model (2PF) CDD [15].

In the figures (1) to (5), we present the dependence of the CDD on r for ^{24}Mg, ^{28}Si, ^{30}Si, ^{32}S and ^{34}S nuclei. The squares are the fitted to the experimental CDD, the dashed curves are the calculated CDD with $\alpha \neq 0$ for the above nuclei.

For all considered nuclei that are under investigation, the experimental values of the root mean square charge radii, the central CDD at $r=0$, the calculated values of the size parameter b, the calculated parameters α, α_1 and α_2 of the 2s-1d shell nuclei are presented in table (1). The occupation numbers of 2s, 1d and 1f orbits of 2s-1d shell nuclei are presented in table (2).

Table (1) Parameters of the CDD of 2s-1d shell nuclei

Nucleus	Model	$\langle r^2 \rangle^{1/2}$ *fm* exp.[9]	$\rho(0)$ $e.fm^{-3}$ exp.[9]	*Z*	*b fm*	α	α_1	α_2
^{24}Mg	2PF	3.03	0.0817	12	1.8554	1.39499	1.39193	3.053×10^{-3}
^{28}Si	MI	3.078	0.0847	14	1.8441	1.36030	1.35745	2.851×10^{-3}
^{30}Si	MI	3.148	0.0763	14	1.8861	1.43175	1.43144	3.078×10^{-3}
^{32}S	MI	3.244	0.090	16	1.9132	0.99223	0.99191	3.255×10^{-4}
^{34}S	MI	3.277	0.0871	16	1.9326	0.99804	0.99476	3.288×10^{-3}

Table (2) Proton occupation numbers of states

Nucleus	Occupation Numbers of 2s	Occupation Numbers of 1d	Occupation Numbers of 1f
^{24}Mg	0.60501	3.39193	3.053×10^{-3}
^{28}Si	0.63970	5.35745	2.851×10^{-3}
^{30}Si	0.56825	5.43144	3.078×10^{-4}
^{32}S	1.00776	6.99191	3.255×10^{-4}
^{34}S	1.00195	6.99476	3.288×10^{-3}

It is evident from figures (1) to (5) of the CDD that the calculated densities with $\alpha=0$ (dashed curves) are in poor agreement with the fitted data, especially for small r. Introducing the parameter α in our calculations, leads to a good agreement, as shown by the solid curve in these figures.

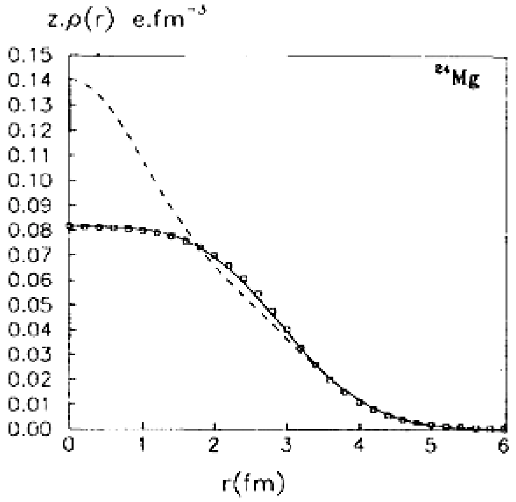

Fig. (1): Dependence of the CDD of ^{24}Mg nucleus on r. the dashed and the solid curves are the calculated CDD of Eq. (7) when $\alpha=0$ and $\alpha\neq0$, respectively. The squares are the fitted to the experimental data of Two Parameter Fermi Model CDD [15] with the parameters $c=2.98$ f_m and $z=0.551$ f_m

Inspection of the CDD of the ^{30}Si and ^{34}S nuclei which are shown in figures (3) and (5), indicate that the additional neutrons to the ^{28}Si and ^{32}S nuclei, lead to change slightly the distribution of the protons in the shells because of the nuclear interactions between these additional neutrons and the protons. This interactions leads to some decrease in the CDD especially at the central regions of these nuclei. By the additional neutrons to these nuclei, the charges are removed from the interior and from the tail of the distributions and transferred into the surface regions.

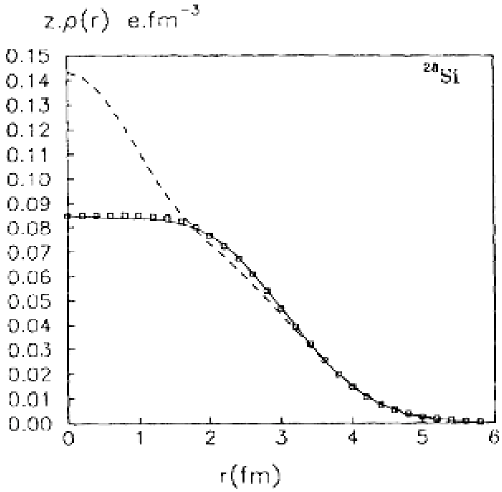

Fig. (2): Dependence of the CDD of ^{28}Si nucleus on r. the dashed and the solid curves are the calculated CDD of Eq. (7) when $\alpha=0$ and $\alpha\neq0$, respectively. The squares are the fitted to the experimental data of Model Independent CDD [9]

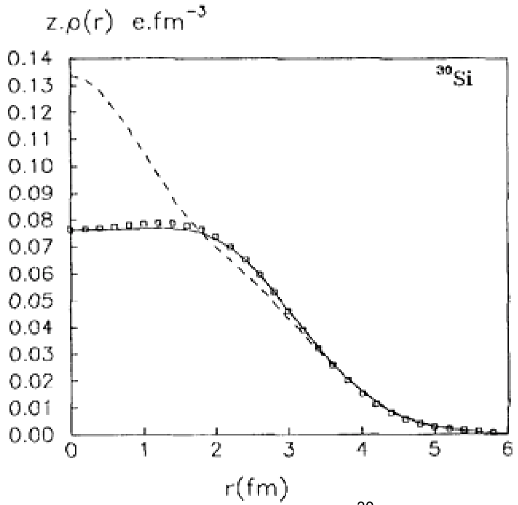

Fig. (3): Same as in Fig. (2) but for ^{30}Si nucleus

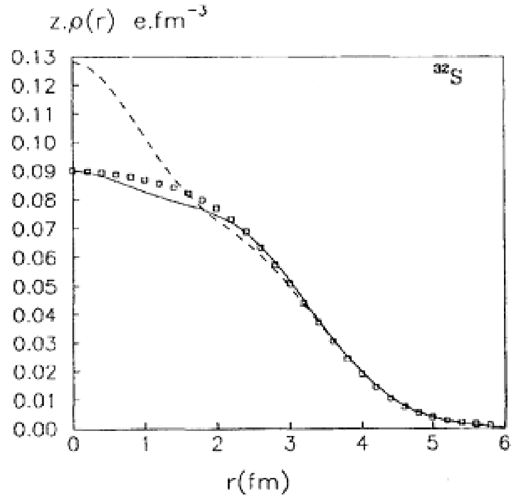

Fig. (4): Same as in Fig. (3) but for ^{32}S nucleus

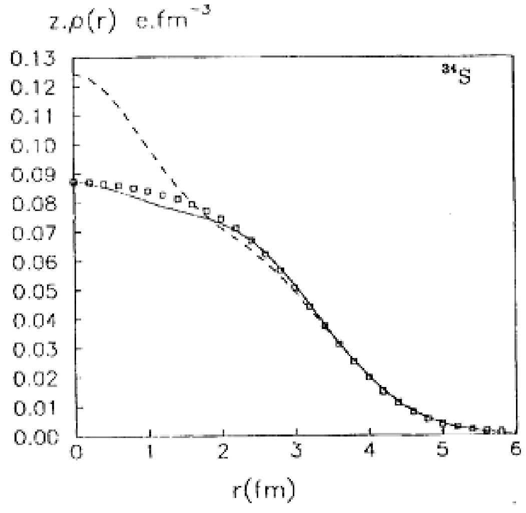

Fig. (5): Same as in Fig. (2) but for ^{34}S nucleus

The difference of the CDD of (^{30}Si-^{28}Si) and (^{34}S-^{32}S) isotopes $\Delta\rho(r)$ are calculated to clarify the influence of the additional neutrons on the CDD as shown in the figures (6) and (7), respectively. The squares are the differences of fitted CDD and the solid curves are the calculated difference of the CDD with $\alpha \neq 0$.

The elastic electron scattering form factors from the considered nuclei are calculated and compared with the experimental data as a function of the momentum-transfer q as shown in the figures (8) to (12), where the circles are the experimental results, squares are the fitted to the experimental data and the solid curves are the calculated results.

The from factors of ^{24}Mg nucleus are presented in figure (8). The experimental data [14] are well described by the calculated data up to $q \approx 3\ fm^{-1}$ as shown by the solid curve. Figures (9) and (10) show the form factors of ^{28}Si and ^{30}Si nuclei, respectively. There is good agreement between the calculated and the experimental data [14] for all momentum transfer values of ^{28}Si nucleus. For ^{30}Si nucleus, the experimental data [16] (circles) are very good described by the calculated data, and the fitted to the experimental data [9] (squares) are described in the region $q \leq 1.45 fm^{-1}$, the second diffraction minimum in the fitted data is also described by the calculated data. The form factors of ^{32}S and ^{34}S are displayed in figures (11) and (12), respectively. The experimental data [16] of ^{32}S nucleus and the fitted data [9] of ^{34}S nucleus are very well explained by our calculated form factors. The calculated form factors slightly dispredicts these data at high q values, and it may be attributed to the necessity of introducing the occupation numbers to the shell 2p.

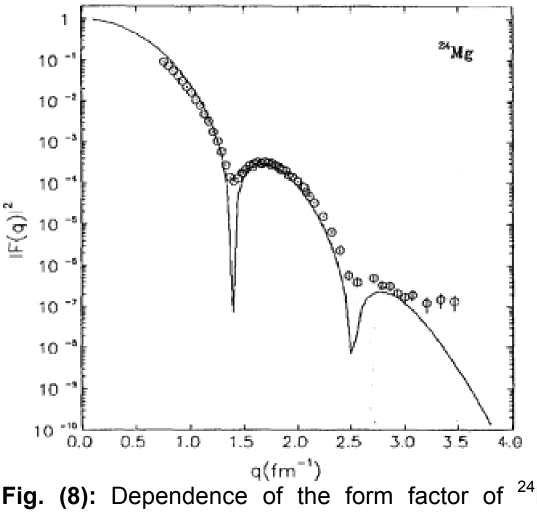

Fig. (8): Dependence of the form factor of ^{24}Mg nucleus on the momentum transfer *q*. The solid curve is the calculated form factor of Eq. (14) with $\alpha \neq 0$. The circles are the experimental data [14]

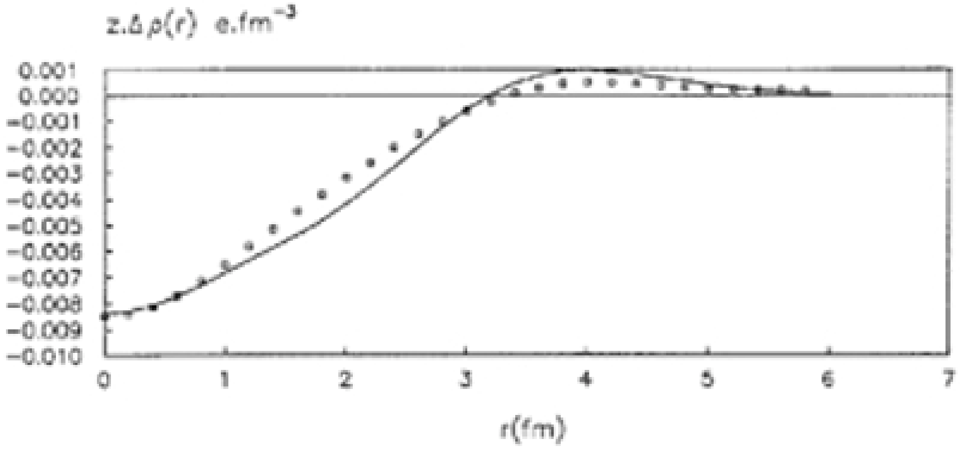

Fig. (6) Dependence of the difference of the CDD of (^{30}Si-^{28}Si) isotopes $Z.\Delta\rho(r)$ on *r*. The squares are the Model-Independent difference of the CDD. The solid curve is the calculated difference of CDD with $\alpha \neq 0$.

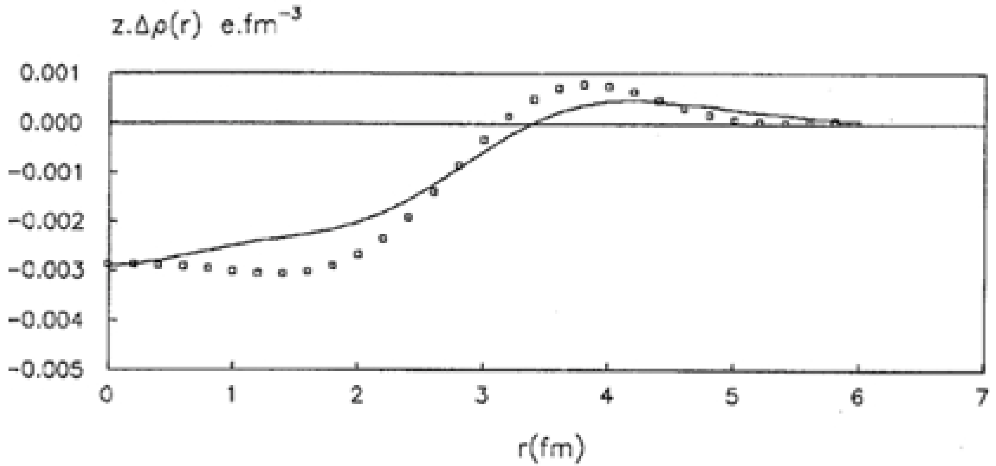

Fig. (7) The same as in Fig. (6) but for (^{34}S-^{32}S) isotopes

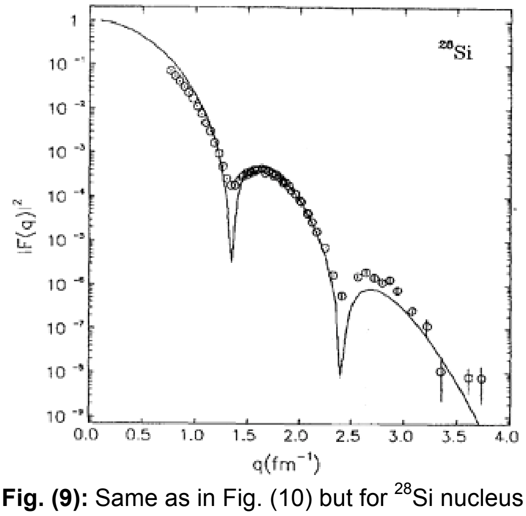

Fig. (9): Same as in Fig. (10) but for ^{28}Si nucleus

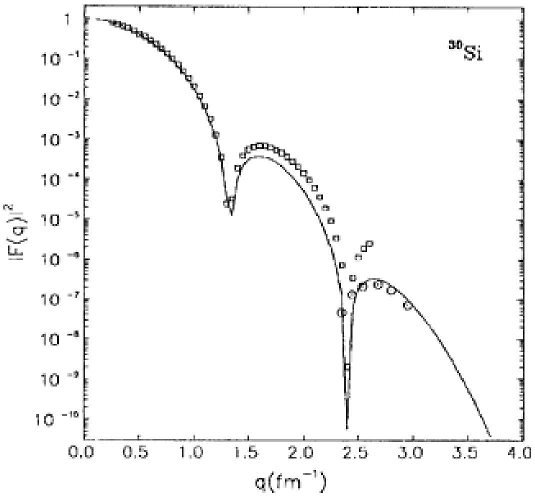

Fig. (10): Same as in Fig. (8) but for ^{30}Si. The circles are the experimental data [16], and the squares are the fitted to the experimental data [9]

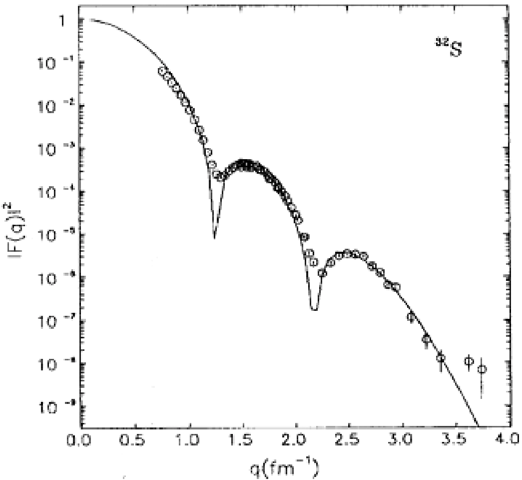

Fig. (11): Same as in Fig. (10) but for ^{32}S nucleus

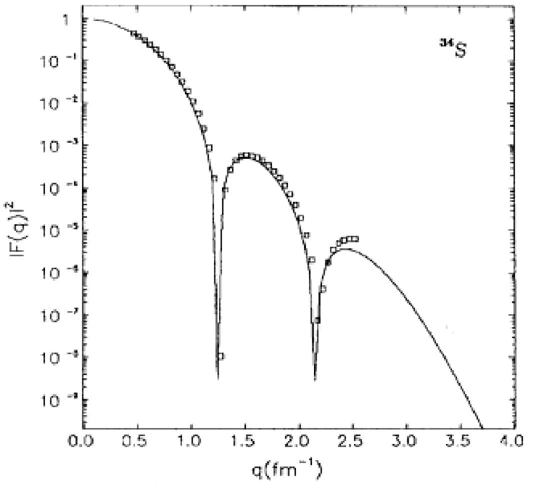

Fig. (12): Same as in Fig. (8) but for ^{34}S. The circles are the experimental data [16], and the squares are the fitted to the experimental data [9]

4. Conclusions

The charge density distribution (CDD) of ^{24}Mg, ^{28}Si, ^{30}Si, ^{32}S and ^{34}S nuclei have been calculated using the wave functions of the harmonic oscillator on the assumption that the occupation numbers of the states in real nuclei differ from the predictions of the simple shell model. The difference of the CDD of (^{28}Si-^{30}Si) and (^{32}S-^{34}S) isotopes have been calculated to clarify the influence of the additional neutrons on the CDD. The elastic electron scattering form factors of the considered nuclei have been calculated using the ground state charge density distributions.

Introducing an additional parameter (α) that reflects the difference of the occupation numbers of states between the real states of the nuclei and the simple shell model predictions, very good agreement between the calculated and experimental results of the CDD and form factors was observed. This leads to the conclusion that proposing (α) as an additional parameter is a real one.

References

[1] Vautherin, D. and Brink, D., *Phys. Rev.* C5 (1972) 626.

[2] Barts, B.I., Bolotin, Yu.L., Inopin, E.V. and Gonchar, V.Yu., "Hartree Fock Method in Nuclear Theory" (in Russian), Kiev, Naukova, Dumka (1982).

[3] Khodel, V.A. and Saperstein, E.E., *Phys. Rep.* 92 (1982) 183.

[4] Saperstein, E.E. and Khodel, V.A., *Sov. J. Nucl. Phys.* 38 (1983) 507.

[5] Antonov, A.N., Hodgson, P.E. and Petkov, I.Zh., "Nucleon Momentum and Density Distribution in Nuclei", Clarendon Press (Oxford) (1988).

[6] Fridrich, J. and Reinhard, P.G., *Phys. Rev.* C33 (1986) 355.

[7] Gul'karov, I.S. and Pinkus, L.D., *Sov. J. Nucl. Phys.* 44 (1986) 210.

[8] Brussard, P.J. and Glaudemans, P.W., "Shell-Model Application in Nuclear Spectroscopy", North-Holland (Amsterdam) (1977).

[9] Atomic Data and Nuclear Data Tables, 36(3), May 1987.

[10] Irvine, J.M., "Nuclear Structure Theory", Pergamon Press (Oxford) (1972).

[11] Lapikas, L., Dieperink, A.E.L. and Box, G., *Nucl. Phys.* A203 (1973) 609.

[12] Chertok, B.T., *Phys. Rev.* 187 (1969) 1340.

[13] Sick, J. and McCarthy, J.S., *Nucl. Phys.* A150 (1970) 631.

[14] Li, G.C., Yearian, M.R. and Sick, I., *Phys. Rev.* C9 (1974) 1861.

[15] Lees, E.W., Curran, C.S., Drake, T.E., Gillespie, W.A., Johanston, A. and Singhal, R.P., *J. Phys.*, G2 (1976) 105.

[16] Wesseling, J. *et al.*, *Phys. Rev.*, C55 (1997) 2773.

This article was reviewed at The Department of Electromagnetism, Faculty of Physics, University of Compostela, SPAIN and School of Applied Sciences, University of Technology, Baghdad, IRAQ

Iraqi J. of Appl. Phys. , Vol. 4 , No. 1 , 2008 , 37-40

Adawiya J. Haider

School of Applied Sciences,
University of Technology,
Baghdad, Iraq
adawiya_haider@yahoo.com

The Effect of Some Experimental Parameters on the Properties of Porous Silicon

The influence of halogen lamp illumination intensity and HF acid concentrations on the properties of n-type porous silicon samples during the light-induced etching process were investigated. The photoluminescence (PL) spectra were recorded for porous silicon samples prepared at high illumination intensity. The peak and the shape of PL spectra are function to illumination intensities. The etching rates and porosities increases with increasing light beam intensity and go through maximum with increasing HF acid concentration.

***Keywords**: Photo-chemical etching, Porous silicon, Photoluminescence*
Received 2 March 2008, Revised 20 March 2008, Accepted 25 March 2008

1. Introduction

Technological application of porous silicon (PS) as a light emitter would have a significant impact on numerous technologies such as display panels or integrated circuits with optoelectronic devices on board. Such devices require strong luminescence intensity. Porous silicon consists of a network of nanometer – sized silicon regions surrounded by void space [1]. In order to obtain PS with desired dimensions and working quantities, electrochemical etching was employed [2-4].

The formation of porous silicon in HF acid with out external biasing (Photochemical etching process) was first reported by Noguchi and Suenume by using a photon such as a high power density laser to supply the required holes in the irradiated area of the silicon wafer to initiate the etching [5]. The illumination wavelength and type of illumination (single wavelength or broad spectra) of the samples during or after the photochemical etching process is known to be an important etching parameter which can be used to modify the morphology and the photoluminescence spectra of the PS [6-8]. The purpose of this work is to prepare a PS and study the role of the halogen lamp illumination intensity and HF acid concentrations on etching rate, porosity and photoluminescence properties of (PS).

2. Experiment

Fig.1 shows a schematic diagram of experimental set-up for photochemical etching process. A commercially available mirror-like n-type (111) oriented wafer of (4.3-5.6)Ω.cm resistivity was rinsed with acetone and ethanol to remove dust and with dilute (HF) to remove the native oxide and then immersed in electronic grade HF acid. The immersed wafer was mounted on two Teflon plates and irradiated at normal incidence on the polished side in a such away that the current could pass from bottom surface to light irradiation area on the top polished surface through the electrolyte as shown in Fig. (1).

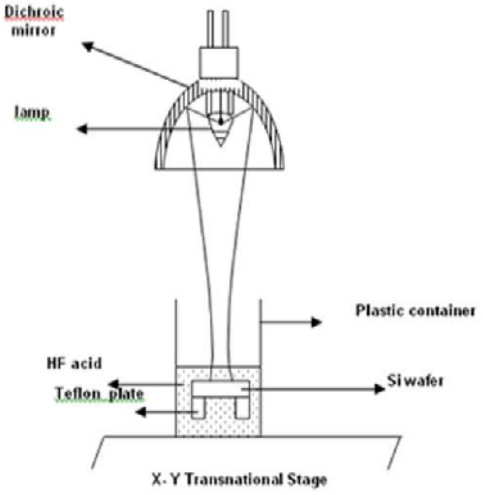

Fig. (1) Experimental set-up for Light-induced etching

In this electrode less photochemical etching process, there was no applied bias. The light beam of quartz Tungsten halogen lamp integral with dichroic ellipsoidal mirror has been focused on a silicon wafer to a circular spot ($0.75 cm^2$) area, the distance between the halogen lamp and the wafer about (4cm). Bubbles were observed during the etching process. Wafers were etched for 10 min at different illumination power and different HF acid concentration I_1=66.7W/cm^2, I_2=133.3W/cm^2, I_3=200W/cm^2 and I_4=333.3W/cm^2 and 10%, 20%, 30% and 40% respectively, after which they were rinsed with ethanol and dried in stream of nitrogen gas. The porous layer was formed on the mirror-like side of wafer. The value of the mean porosity over the thickness of PS layer and the thickness of PS layer were determined gravimetrically. Photoluminescence measurement was done by using He-Cd laser at a wavelength of 325nm with a low laser power density of nearly 10 mW/cm^2 in the School of Physics, Nanostructures and Optoelectronics Research Center (NOR Lab) at the University Sian in Malaysia.

3. Results and Discussion

Fig. (2) shows the relationship between the light beam intensity and the etching rate. The rates were estimated from dividing the porous layer thickness by the etching times. We can easily distinguish two regions: one at intensity up to 200W/cm^2 there is a relatively large increase in the etching rate, while the second at higher intensities, the etching rate tends to saturate (level up). The change in the slope indicates most probably a change in the reaction mechanism [9].

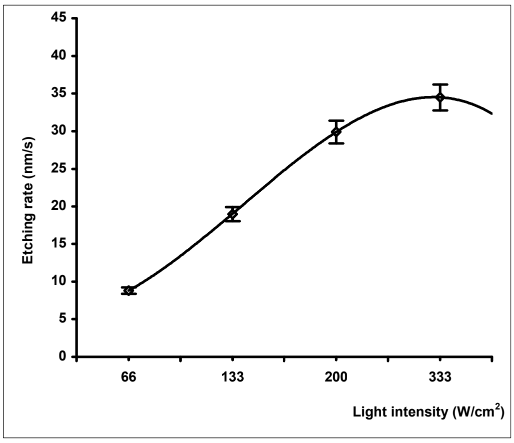

Fig. (2) the effect of light beam intensity on the etching rate of silicon nanocrystilities (nc-si), ρ=(4.3-5.6)Ω.cm

This increasing in the etching rate is due to the photon absorption of the ordinary etching light with it, larger band width from near infrared region to visible where the peak of the lamp emission around (λ=0.9μm) and this will provide a good absorption due band to band transition and also due the absorption by the impurities especially at the larger wavelengths, the absorption length which is depended on the wave length of the light is varied from (sub μm to few μm) [10], this will lead to hole formation at a different depth from the polished surface and depletion layer will form in the silicon wafer such that the polished surface is relatively positive while the back side of the wafer is negative. This created a net flow of charges from the negative to the positive side resulting in a current flow which will be completed by ions flowing in the HF solution. This net perpendicular flow of charges across the wafer will encourage the etching rate in the direction of the illumination [2, 11].

Figure (3), shows that, at a given intensity, the etching rate goes through a maximum as the HF acid concentration is increased, the maximum occurring at an HF acid mass concentration of around 30%. As the concentration of HF acid increases, there are more electron accepters in the solution, resulting in an increased rate of charge transfer between the semiconductor surface and the electrolyte [9]. Thus, band bending is larger at higher HF acid concentrations. For highly concentrated solutions of HF acid, more than 30%wt, band bending is reduced by formation of ion complexes in the solution [9, 11].

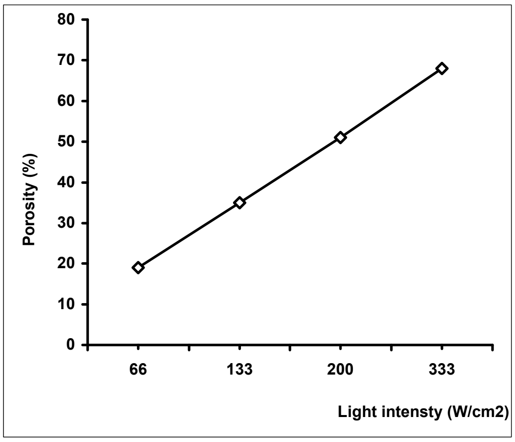

Fig. (3) The effect acid concentration on nanocrystilities (nc-si), ρ=(4.3-5.6)Ω.cm

Figure (4) shows the relationship between the light beam intensity and the porosity of the resulting porous silicon. The increasing in the illumination intensity is associated by increasing the porosity of the porous layer in approximately a linear relation this behavior is related to the silicon dissolution in the porous layer with increasing intensity [12].

Figure (5), illustrates the photoluminescence spectra of the porous silicon samples, the spectra were recorded for samples illuminated by different light beam intensity (I) 50, 100, 150, 250 and 30% HF acid concentration. The PL spectra were not obvious at low pumping intensity while are clear at high rate I_2 to I_4. These behaviors reflect the nature of the porous layer especially the morphological case.

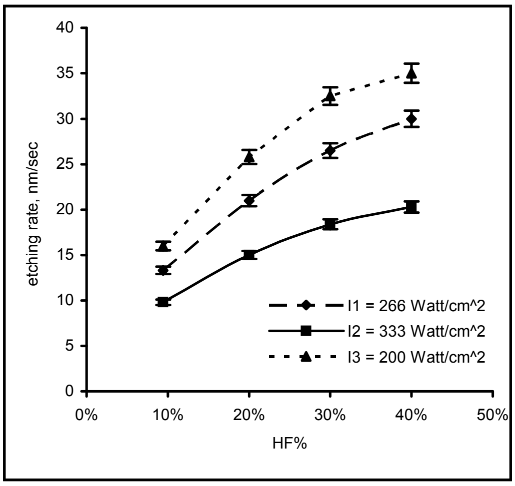

Fig. (4) The effect of light beam intensity on the porosity of PSi

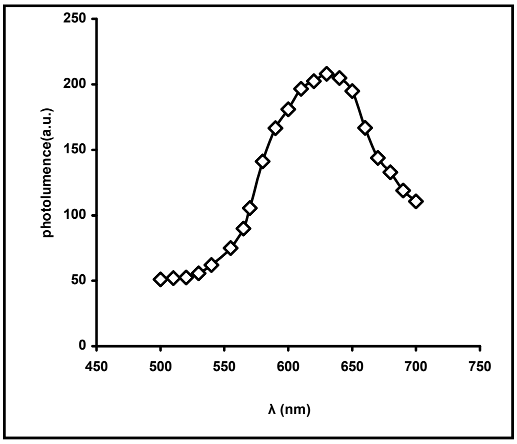

Fig. (5) PL for PS Prepared under 100W and 30% HF concentration

At low illumination intensity the porous layer may contain disconnected pits and these pits are commenced with the initiation of etching process on silicon wafers, i.e. the samples has low porosities, i.e., large size of nanocrystilities. Increasing the illumination intensity will increase the number of these pits leading to form a porous structure, [11] this structure was clear at the samples with high porosity. The increasing the porosity in porous silicon with I_2 illumination samples lead to form the nano-scale silicon [1,13-15] .In this type of silicon the photoluminescence properties at room temperature is recorded by many authors [1,8,15]. The peak of PL prepared in illumination in Fig. (6) is about (360eV) while at I_3 illumination intensity is blue shifting to (229eV). This is attributed to size of silicon nanocrystilities, according to quantum confinement (QC) effects [15], and

$$E_{g_{new}} = E_{g_{bulk}} + \frac{88.34}{L^{1.37}} \qquad (1)$$

the average nano-size is (2.006eV) for Fig. (6) and (2eV) for Fig. (5).

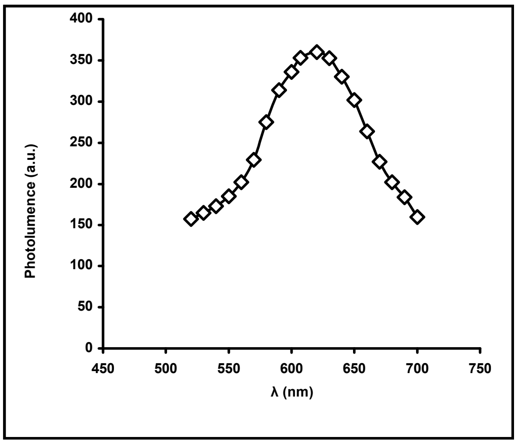

Fig. (6) PL for PS Prepared under 150W and 30% HF concentration

As shown in Fig. (7), the PL properties for samples shows in addition to the blue shifting, presses a new peak at (2.1eV) in addition to the (3.03eV) peak. This behavior refers to form a double porous layer one at low nano-size a bout (410nm) and another at (580nm). This may due to the excessive etching of the first layer leading to form small nano-size. This layer may presses at the surface of PS layer [12,15].

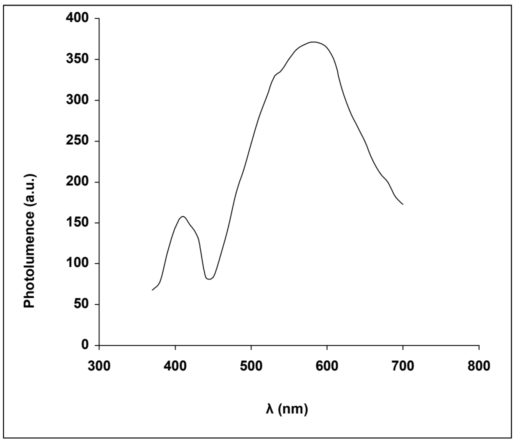

Fig. (7) PL for PS Prepared under 250W and 30% HF concentration

4. Conclusion

The variation of the HF acid concentration and illumination intensity during porous silicon formation causes dramatic changes in the porous silicon properties. We found that the etching rates and the porosity of the porous layer increases with illumination intensity of the halogen lamp and go through maximum with increasing HF acid concentration. The main reason for increasing the etching rate and hence the porosity might be related to electron hole generation by the light radiation and transport holes to the surface .the PL spectra is observed just from the porous silicon samples at high illumination intensities only. The PL spectra this may relate to the fact that at high porosities the amount is a function to the illumination intensity with a blue shifting.

Acknowledgement

The author is grateful to Dr. N.M. Alrawi for the measurement facilities, as well as to Prof. A.M.I. Ahmed and A.M. Alwan for many useful discussions.

References

[1] L.T. Canham , *Appl. Phys. Lett.*, 57 (1990) 1046.
[2] M.I.J. Beale et al., *J. Cryst. Growth*, 73 (1985) 622.
[3] H. Gerischer and M. Lübke, Ber. Bunsen-Ges, *J. Phys. Chem.*, 91 (1987) 394.
[4] V. Lehmann, *J. Electrochem. Soc.*, 140 (1993) 2836.
[5] N. Nouguchi and I. Suemune, *Appl. Phys. Lett.*, 62 (1993) 1429.
[6] V. Lehmann, H. Cerva and U. Gosele, *Mater. Res. Soc. Symp. Proc.*, 256 (1992).
[7] M. Thonissen et al., *Thin Solid Films*, 276 (1996) 21.
[8] H. Mavi et al., *J. Non-Cryst. Solids*, 162 (2001) 286.
[9] P. Lim, J. Brock and I. Trachtenberg, *Appl. Phys. Lett.*, 60(4) (1992) 27.
[10] D.E. Aspen and A.A. Studna, *Phys. Rev. B.*, 27 (1983) 985.
[11] L. Koker and K.W. Kolasinki, *J. Phys. Chem.*, 2 (2000) 277.
[12] B.G. Rasheed, "Spectroscopy of Porous Silicon Prepared By Laser-Induced Etching", PhD thesis, Indian Institute of Technology, Delhi, India (2003).
[13] C. Peng and K. Hirschman, *J. Appl. Phys.*, 80 (1996) 295.
[14] N. Lalic, "Light Emitting Devices Based on Silicon Nanostructures", PhD thesis, KTH, Royal Institute of Technology, Stockholm (2000).
[15] L. Canham, **"Properties of Porous Silicon"**, INSPEC (U.K.) 2004.

This article was reviewed at School of Electrical and Electronic Engineering, Nanyang Technological University, SINGAPORE, Department of Applied Physics, Ministry of Science and Technology, IRAQ, and School of Applied Sciences, University of Technology, Baghdad, IRAQ

Moath N. Hussain
Jasim M. Abdul-Jabbar

[1] *Department of Electronic and Communications Engineering, College of Engineering, University of Basrah, Basrah, Iraq*

Fabrication and Characterization of InZnO TFTs Grown on Transparent Conductive Oxide Substrate by DC Sputtering Technique

In this work, depletion-mode transistors were made of InZnO thin films prepared and grown on transparent conductive substrates by DC sputtering technique. The SiO_2-In_2O_3-ZnO system and N_2 plasma incorporated InZnO film were grown to get a better controllability of the carrier concentration during the film growth. Hydrogen plasma and oxygen plasma effects on the TCO films and the TFTs were investigated. Devices were simulated in a device model to extract the parasitic parameters. The depletion-mode TFTs have been fabricated successfully on glass by using InZnO films as the channel layers.

Keywords**:** InZnO films, Thin film transistor, TCOs, DC sputtering
Received: 22 December 2009, **Revised**: 04 February 2010, **Accepted**: 11 February 2010

1. Introduction

Flexible electronics is emerging rapidly [1,2]. Theses devices have the advantages such as low profile, light weight, small size, and better performance. In displays, thin film transistors (TFTs) are used as switching components in the active-matrix over a large area. Currently, liquid crystal displays (LCDs) mostly use amorphous Si as the channel.in TFTs. However, due to the low mobility (<1cm^2/Vs) and high process temperature (350°C), amorphous Si-TFTs are not available for high resolution displays on cheap plastic substrates. Organic TFTs have very low mobility (<1cm^2/Vs) and may have reliability concerns [3]. Oxide-based TFTs have at least 1 order higher mobility (10~50cm^2/Vs) [4] than amorphous Si-TFTs and organic TFTs and can be deposited at room temperature. The high mobility of oxide-based TFTs, make them available for high resolution displays and can integrate switching TFTs in the active-matrix and driver-integrated circuits (driver ICs) on the same plastic substrate, which can reduce cost and provide a more compact display. Besides, oxide-based TFTs have other advantages such as room temperature deposition, higher transparency, better smoothness, etc. [5]. The oxide-based TFTs have a great potential to realize a roll-to-roll display. If this technology can be realized, it may not only replace the current amorphous Si-TFTs for LCDs, but will also create new applications on various sets such as heads-up, windshield, electronic books or light weight computers for soldiers in the battle field and eventually change the whole display industry.

In this study, we fabricated TFTs by sputtering InZnO and InGaZnO on hard (glass) and flexible (plastic) transparent substrates. Depletion mode and enhancement mode field effect transistors will be fabricated. The study will include device designs, materials tuning, process developments, device characterization, device simulation, device reliability test, and device circuit demonstration. The study will cover the whole course of the device development.

TCOs are composed of post-transition metal oxides with outer major quantum number nγ4. These TCOs exhibit n-type carriers [6]. Oxygen vacancies dominate the carrier concentration in these TCO films. For these TCOs, the mobility is still close to that of the polycrystalline even in the amorphous material. It is very different fromα-Si, which has a extremely low mobility (<1cm^2/Vs) in amorphous type comparing to the several orders higher mobility in polycrystalline (30-300cm^2/Vs) or crystalline (>1000cm^2/Vs) [3]. Although there is more than one mechanism explaining the conduction behavior for these TCOs, the most widely accepted theory of carrier transport is the s orbitals overlapping of these transition metal atoms [6].

Many groups reported oxide based TFTs using InZnO, GaZnO, ZnO, SnO_2, In_2O_3 as channel layers fabricated on glass [7-10]. However, few of them are reported on organic flexible transparent substrates. In recent years, α-

Si TFTs have been fabricated a lot on organic substrate such as PET (polyethylene terephthalate) [11]. Recently, an enhancement mode TTFT using IGZO as the channel layer and Y_2O_3 as the gate dielectric fabricated on a PET substrate was reported [12-14]. The TFT has a field effect mobility of $10cm^2/Vs$, threshold voltage 1.2V, on-off ratio $>10^6$, subthreshold voltage swing ~0.2V/decade. It shows the TCO type TFTs have great potential to beat theα-Si TFTs (low mobility $<1cm^2/Vs$, high temperature 350°C) and organic TFTs (low mobility $<1cm^2/Vs$) [3] not only in electrical properties, but also in optical properties, ease of processing, and cost.

Currently, two different technologies are used to fabricate TFTs on plastics. The first one is to deposit films and do processes directly on the plastics [15]. The other one is to fabricate TFTs on rigid glass first, then etch off the substrate glass and paste the flexible plastics onto the TFTs [16]. The second one can avoid high temperature and stress caused by film deposition. However, our InZnO and InGaZnO TFTs are fabricated in a room temperature process, so we can use the direct process approach.

2. Experiment

We plan to fabricate the depletion mode TTFTs as shown in Fig. (1a). The gate dielectrics will be SiO_2, SiN_x or Sc_2O_3. Channel layers will be InZnO or InGaZnO. Device performance will be compared for different structures. Eventually, a fully transparent TFT will be fabricated on a flexible transparent substrate, PET.

We have already fabricated depletion mode thin film transistors using InZnO as the channel layer on glass substrates as depicted in Fig. (1b). This is the first report of depletion mode TFTs made of InZnO film in channel layer [17]. The InZnO films were deposited near room temperature by rf magnetron sputtering using 4in. diameter targets of In_2O_3 and ZnO [18]. The working pressure was varied from 2-15mTorr in a mixed ambient of O_2/Ar. The percentage of O_2 in the mixture was varied from 0-3%. At a percentage of 2.5%, we obtained films with carrier concentration of $\sim10^{18}cm^{-3}$ and electron mobility of $17cm^2.V^{-1}.s^{-1}$ obtained from Hall measurements. The partial pressure of oxygen during the sputter deposition was found to be the dominant factor controlling the conductivity of the films. The sputtering power on the targets was held constant at 125W, leading to compositions of the films measured by x-ray fluorescence spectroscopy of In/Zn=0.5 in atomic ratio. The typical thickness of the InZnO films deposited was 150nm, with a root mean square roughness of 0.4nm measured over a $10x10\mu m^2$ area by Atomic Force Microscopy. The films were amorphous as determined by x-ray diffraction and showed optical transmittance of ~80% in the visible range.

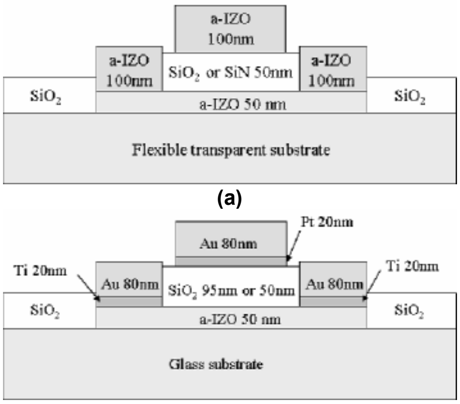

(a)

(b)

Fig. (1) (a) Schematics of the fully transparent D-Mode TFTs on flexible transparent substrate. (b) D-Mode TFTs on glass

As described in the previous section, the InZnO film was deposited in the sputtering machine with two targets, ZnO and In_2O_3, together with O_2 and Ar gas in the chamber. The O_2/Ar ratio decides the carrier concentration in the InZnO film. Here we plan to use N_2/O_2/Ar gas mixture to deposit InZnO film. The reasons to use N_2 is because in the plasma, N_2 will convert to N_2^+, which may replace O and bond with In. This was investigated in forming p-type ZnO [19]. We know the carriers in the InZnO result from the non-stoichiometry, which means the lack of oxygen allows some indium atoms that are not bonded with oxygen atoms to release electrons to the conduction band. That is why when the O_2/Ar ratio change during InZnO film deposition, the carrier concentration will also change. Higher O_2/Ar ratio leads to a decrease in the number of oxygen vacancies, which also means the carrier concentration decreases [18]. When removing one oxygen atom from the indium, one oxygen vacancy is created. In is a big atom and tends to lose electrons. Oxygen is a small atom and tends to get electrons from the In. ZnO acts as a stabilizer in the In_2O_3 matrix. That's why InZnO and GaZnO both have lower sensitivity of O_2/Ar ratio to carrier concentration than ZnO [10]. Since the oxygen has a higher electronegativity than nitrogen, oxygen can form a strong ionic bond with In. This means when removing or adding a certain amount of oxygen or nitrogen bonded with indium, oxygen will produce a larger change in carrier concentration than nitrogen. This means nitrogen can reduce the sensitivity of O_2/Ar ratio to carrier concentration. The second reason is, due to the previous reason, nitrogen may improve the device reliability. A reliability issue is one of the reasons why GaInZnO was developed [14]. We may provide another view to do the same thing by an easier method.

Ga_2O_3 introduced into the In_2O_3-ZnO system to form the InGaZnO was reported as providing a better stabilization in TFTs than InZnO [14]. Ga was chosen because it has an atomic radius close to In. The introduction of Ga into the InZnO reduces the electron concentration and mobility. The highest carrier concentration of InGaZnO is around $\sim10^{19}cm^{-3}$ [12] which is smaller than that of InZnO ($\sim10^{21}cm^{-3}$) [10]. The reduction in carrier concentration is not bad because for the channel layer, $10^{18}\sim10^{16}cm^{-3}$ is enough for both depletion and enhancement mode TFTs. Although carrier concentration in InZnO can also be adjusted by O_2/Ar ratio, the carrier concentration change in the InZnO film is dramatic ranging from 10^{18} to $10^{16}cm^{-3}$ in a small O_2/Ar ratio region [18]. Ga not only reduces carrier concentration, but also reduces the sensitivity of the carrier concentration to the O_2/Ar ratio [10,12]. It is good for controlling the carrier concentration. However, in the mean time, the reduction in mobility is not welcome. It is interesting to introduce another oxide into the InZnO system to stabilize the oxide system and the mobility. The idea is to incorporate a smaller atom and in the mean time, oxide formed by this atom has E_g>3eV. SiO_2 fits these requirements. Si can easily bond with oxygen to reduce sensitivity of the carrier concentration to the O_2/Ar ratio during film deposition. Also, due to the smaller radius of Si than Ga, In atoms still can keep their s orbitals overlapped. This means the mobility may not be degraded too much.

Due to the different interfaces that may form between InZnO and various dielectrics, it is necessary to use different dielectrics such as SiO_2, SiN, and Sc_2O_3 as the gate dielectrics in the TFTs and compare the device performance.

O_2 plasma can obviously decrease the surface carrier concentration of the InZnO film due to the annihilation of the oxygen vacancies. This might help to reduce the surface leakage and then improve on/off ratio if the surface leakage dominates the leakage current, especially for the depletion mode FET. H^+ was reported to be implanted into the $CdO-CeO_2$ film and act as a shallow donor [20]. We believe that H_2 plasma can also create a donor in InZnO film. One very interesting experiment is that to be easier to control the carrier concentration by hydrogen plasma if we introduce hydrogen into an InZnO film, which had been deposited under a high O_2/Ar ratio. Due to the very small size of the hydrogen, it should not reduce the hall mobility of the InZnO film because it will not inhibit the overlap of the 5s orbitals of In.

After we successfully fabricate the D-mode FETs, we can start to make a ring oscillator using these TFTs. The reliability test will include (i) current stress in room temperature and high temperature (ii) thermal shock and bending test. These tests will be applied to the TCO films and devices on both glass and PET. The device will also be measured for the s parameters and be simulated to extract the parasitic parameters of the D-mode FETs. We have already performed the simulation for the D-mode InZnO TFTs, which will be mentioned in the latter section. TFTs made of InZnO, InGaZnO will be compared and discussed.

An Agilent 4156 parameter analyzer and Agilent E8361 network analyzer will be used to characterize the device dc and rf performance, respectively.

3. Results and Discussion

Top-gate-type TFTs using a-InZnO channels and 50nm or 95nm thick SiO_2 gate insulators deposited by plasma enhanced chemical vapor deposition were fabricated as shown schematically in Fig. (1a). Figure (2) shows the top-view of the TFT. The gate dimension is 36μm×100μm. The InZnO film deposited in 2.5% O_2/Ar ratio has a carrier concentration about $10^{18}cm^{-3}$ [18]. The whole process was done without heating the substrates, making the entire process consistent with typical continuous-use temperatures of commercial plastic films for electronic devices.

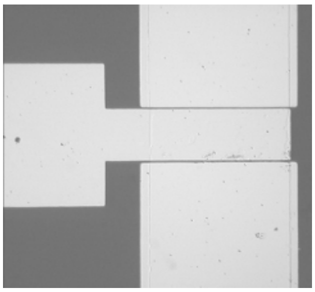

Fig. (2) Top-view of the TFT

Figure (3) shows I_{DS}-V_{DS} characteristics from InZnO transistors with 50nm thick SiO_2 gate dielectric. The transistor operates in depletion-mode with an appreciable drain current at zero gate voltage and exhibits excellent drain current saturation.

Figure (4) shows I_{DS} and g_m as a function of V_{GS} for a device with 50nm SiO_2 gate. The sub-threshold voltage swing was 1.9V/decade and the device had a threshold voltage of -6.5V.The latter is the gate voltage at the onset of the initial sharp increase in current in log(I_D)-V_{GS} characteristics. The drain current on-to-off ratio was >10^6. These results are competitive with past results on TFTs using room temperature sputter deposited amorphous $InGaZnO_4$ as the channel material [5]. The field-effect mobility was of ~4.5cm^2.V^{-1}.s^{-1}.

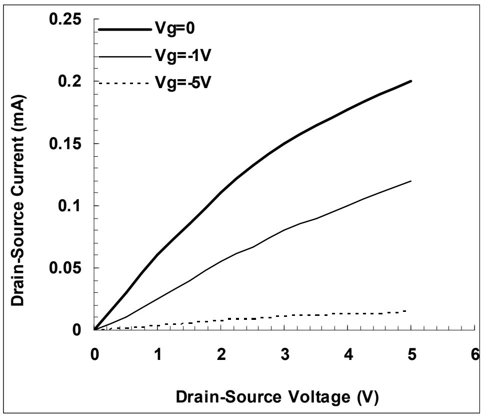

Fig. (3) I_{DS}-V_{DS} characteristics from InZnO transistors with 50nm thick SiO_2 gate dielectric

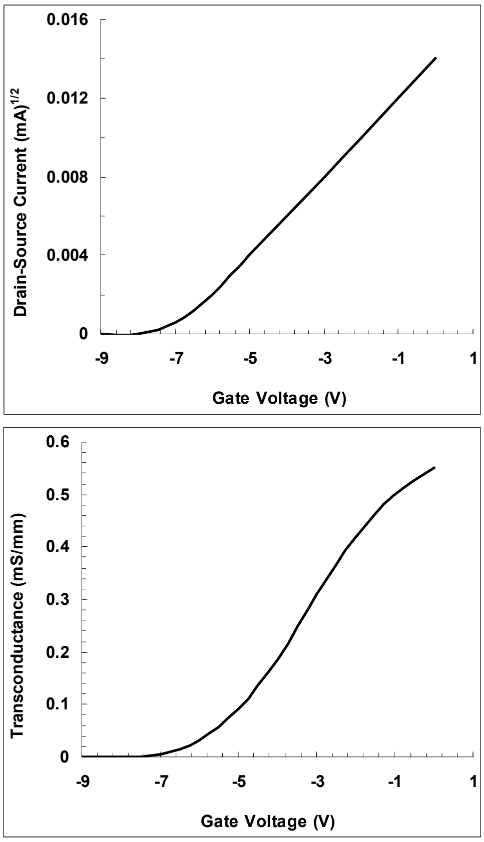

Fig. (4) Drain-source current (I_{DS}) and transconductance (g_m) as a function of V_{GS} for a device with 50nm SiO_2 gate

The gate I-V characteristics from devices with two different gate dielectric thicknesses are shown in Fig. (5). The leakage current is very small, in the 10^{-10}A range, for both gate thicknesses and demonstrates that the low temperature deposition process produces acceptable quality SiO_2 for TFT applications. The threshold voltage was decreased to -5.5V for the thicker dielectric and the slope of the subthreshold voltage swing was 0.87V/decade for the 95nm thick dielectric.

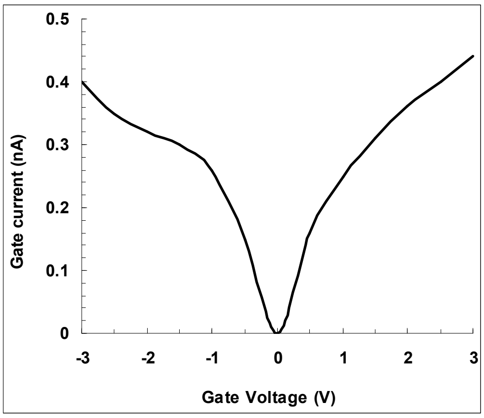

Fig. (5) The gate leakage current characteristics of the devices with two different gate dielectric thicknesses

Top-gate TFTs using 50nm of α-InZnO channels and 12.5nm-thick SiN_x gate insulators deposited by chemical vapor deposition (CVD) were fabricated as shown similarly in Fig. (1b). The gate dimension is 1µm×200µm. The SiN_x layer was deposited without heating the substrates. In addition, the SiN_x gate dielectric provided superior stability of device performance relative to SiO_2 deposited under the same conditions [17]. Specific contact resistance and sheet resistance from the linear transmission line measurements were $7\times10^{-5}\Omega.cm^2$ and 0.9MΩ/sq, respectively. Figure (6) shows typical drain current versus drain voltage, I_{DS}-V_{DS}, characteristics from the InZnO transistors.

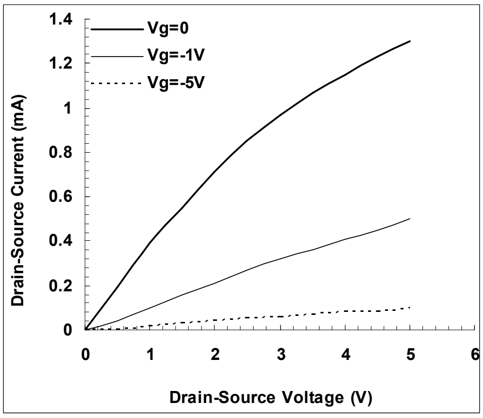

Fig. (6) Typical drain current versus drain voltage, I_{DS}-V_{DS}, characteristics from the InZnO transistors

Figure (7) shows drain current, I_{DS}, and transconductance, g_m, as a function of V_{GS} for an InZnO TFT. A maximum transconductance of 7.5mS/mm was obtained at I_{DS}=1.35mA, V_g=0V and V_d=5V. This is the highest transconductance ever reported for InZnO based TFTs. The transistor has a low threshold voltage of -2.5V. The drain current on-to-off ratio was >10^5. The gate leakage is about 10^{-10}A~10^{-11}A. The field-effect mobility is 14.5cm^2.V^{-1}.s^{-1}.

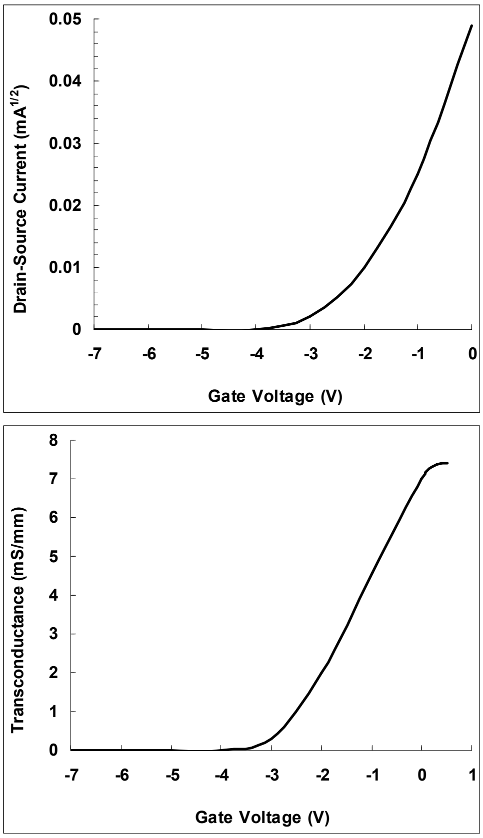

Fig. (7) drain current (I_{DS}) and transconductance (g_m) as a function of V_{GS} for an InZnO TFT

The measured s-parameters, estimated h_{21} and unilateral power gain of a typical InZnO TFT are illustrated in Fig. (8) and Fig. (9), respectively. The TFT was biased at drain and gate voltage of 3V and 0V, respectively during the s-parameter measurements. Unity gain cut-off frequency and maximum frequency of oscillation of 180MHz and 155MHz, respectively, were achieved.

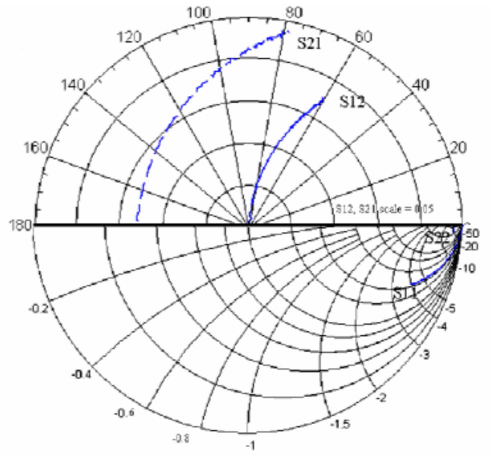

Fig. (8) The measured s-parameters of a typical InZnO TFT

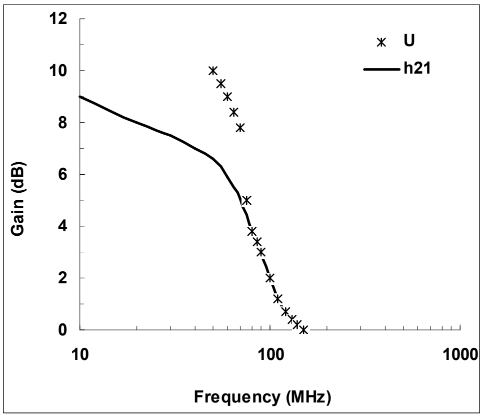

Fig. (9) The estimated (*h₂₁*) and unilateral power gain (U) of a typical InZnO TFT

A simplified equivalent T-model for the InZnO TFT, as shown in Fig. (10), was used to extract the device parameters. The extracted device parameters are listed in Table (1). The extracted source and drain resistance were consistent with the estimated resistance based on the transmission line measurements and drain I-V characteristics. The simulated intrinsic transconductance was very close to the measured extrinsic transconductance. The low cut-off frequency of the InZnO was limited by the fairly long transit time, 16ps, low transconductance, and high parasitic resistances, which were results of the low mobility and saturation velocity of the α-InZnO channel layer. However, this MHz-range switching performance is sufficient for many display applications.

An amorphous or polycrystalline Si:H layer as the channel have been commonly used for most conventional TFTs in display applications. The standard Si-based TFTs have drawbacks such as light sensitivity, light-induced degradation and low field effect mobility (<1cm^2/Vs) [3]. Therefore, Si:H TFT devices reduce the efficiency of light transmittance and brightness. Besides, both amorphous and polycrystalline Si:H TFTs require relatively high process temperatures (350°C and 450°C, respectively) [3] making it difficult to fabricate these TFTs on plastics. One of the methods to increase the efficiency and avoid high temperature is to use amorphous transparent oxides for the channels and electrodes, and fabricate TFTs at room temperature. Table (1) shows the major differences among α-InZnO, α-Si, and polycrystalline Si. Obviously, α-InZnO has the advantages of high field effect mobility, high transparency, room temperature compatible processing, large area deposition by sputtering, plastics substrate available, and is a cheaper process [3].

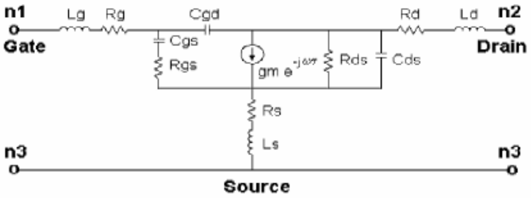

Fig. (10) A simplified equivalent T-model for the InZnO TFT

Table (1) Materials for TFTs used in display applications

Film type	**α-InZnO Amorphous**	**α-Si Amorphous**	**Poly-Si Polycrystalline**
Field effect mobility ($cm^2V^{-1}s^{-1}$)	10-50	0.5-1	30-300
Process temperature (°C)	20	350	450
Transparency (%)	>80	<20	<20
Substrate	Glass plastics	Low cost glass	Quartz

4. Conclusion

In this proposal, InZnO and InGaZnO were used as channel layers to fabricate depletion-mode TFTs and ring oscillators on glass and flexible transparent substrate (PET). The SiO_2-In_2O_3-ZnO system and N_2 plasma incorporated InZnO film were grown to get a better controllability of the carrier concentration during the film growth. Hydrogen plasma and oxygen plasma effects on the TCO films and the TFTs were investigated. The device reliability were tested to compare the effects from different TCO films and process treatments. Devices were simulated in a device model to extract the parasitic parameters. Devices were characterized in DC performance. The depletion-mode TFTs have been fabricated successfully on glass by using InZnO films as the channel layers.

References

[1] K.J. Allen, *Proc. IEEE*, 93 (2005) 1394.
[2] K. Jain *et al.*, *Proc. IEEE*, 93 (2005) 1500.
[3] Y. Sun and J.A. Rogers, *Adv. Mater.*, 19 (2007) 1897.
[4] H.C. Pan *et al.*, *J. Vac. Sci. Technol.*, A 23 (2005) 1187.
[5] T. Sasabayashi *et al.*, *Thin Solid Films*, 445 (2003) 219.
[6] M. Orita *et al.*, *Phil. Mag. B*, 81 (2001) 501.
[7] N.L. Dehuff *et al.*, *J. Appl. Phys.*, 97 (2005) 064505.
[8] R.E. Presley *et al.*, *J. Phys. D: Appl. Phys.*, 37 (2004) 2810.
[9] Dhananjay and C.W. Chu, *Appl. Phys. Lett.*, 91 (2007) 132111.
[10] R. Martins *et al.*, *J. Appl. Phys.*, 101 (2007) 044505.
[11] A. Sazonov and C. McArthur, *J. Vac. Sci. Technol.*, A 22 (2004) 2052.
[12] H. Hosono, *J. Non-Cryst. Solids*, 352 (2006) 851.
[13] K. Nomura *et al.*, *Jpn. J. Appl. Phys.*, 45 (2006) 4303.
[14] T. Kamiya *et al.*, *J. Electroceram.*, 17 (2006) 267.
[15] M.J. Lee, C.P. Judge and S.W. Wright, *Solid-State Electronics*, 44 (2000) 1431.
[16] K. Takechi *et al.*, *IEEE. Trans. Semi. Manuf.*, 18 (2005) 384.
[17] Y.-L. Wang *et al.*, *Appl. Phys. Lett.*, 90 (2007) 1.
[18] W. Lim *et al.*, *Electrochem. Solid-State Lett.*, 10 (2007) H267.
[19] C.L. Perkins *et al.*, *J. Appl. Phys.*, 97 (2005) 034907.
[20] S. Narushima *et al.*, *J. Non-Cryst. Solids*, 374 (2000) 313.